SPECTRAL CHARACTERISTICS OF EARTH-SPACE PATHS AT 2 AND 30 GHz

Robert A. Baxter
Daniel B. Hodge

The Ohio State University

ElectroScience Laboratory

Department of Electrical Engineering
Columbus, Ohio 43212

Technical Report 784299-7

August 1978

Prepared for
National Aeronautics and Space Administration
GODDARD SPACE FLIGHT CENTER
Greenbelt, Maryland 20771

TECHNICAL REPORT STANDARD TITLE PAGE

1. Report No.	2. Government Accession No.	3. Recipient's Catalog No.

4. Title and Subtitle	5. Report Date
SPECTRAL CHARACTERISTICS OF EARTH-SPACE PATHS AT 2 AND 30 FHz	August 1978
	6. Performing Organization Code
7. Author(s) Robert A. Baxter & Daniel B. Hodge	8. Performing Organization Report No. ESL 784299-7
9. Performing Organization Name and Address The Ohio State University ElectroScience Laboratory, Department of Electrical Engineering, Columbus, Ohio 43212	10. Work Unit No.
	11. Contract or Grant No. NAS5-22575
	13. Type of Report and Period Covered Type II Technical Report
12. Sponsoring Agency Name and Address NASA, GSFC Greenbelt, Maryland 20771 E. Hirschmann, Code 951, Technical Officer	14. Sponsoring Agency Code

15. Supplementary Notes

This material was also used as a thesis submitted to The Ohio State University

16. Abstract

In recent years, communication system designers have pushed operating frequencies higher and higher in an effort to meet increasing bandwidth requirements for extremely fast data rates. However, these high operating frequencies are accompanied by increased signal scintillation, especially at low elevation angles on earth-space paths. In this study, spectral characteristics of 2 and 30 GHz signals received from the Applications Technology Satellite-6 (ATS-6) are analyzed in detail at elevation angles ranging from 0^{o} to 44^{o}.

The spectra of the received signals are characterized by slopes and break frequencies. Statistics of these parameters are presented as probability density functions. Dependence of the spectral characteristics on elevation angle is investigated. The 2 and 30 GHz spectral shapes are compared through the use of scatter diagrams.

(over)

17. Key Words (Selected by Author(s))	18. Distribution Statement

19. Security Classif. (of this report)	20. Security Classif. (of this page)	21. No. of Pages	22. Price*
U	U	80	

*For sale by the Clearinghouse for Federal Scientific and Technical Information, Springfield, Virginia 22151.

Th
eory.
eory,
tion

TABLE OF CONTENTS

Chapter		Page
I	INTRODUCTION.	1
II	THEORETICAL BACKGROUND.	3
III	EXPERIMENT DESCRIPTION.	10
IV	THE DATA.	17
V	RESULTS.	43
VI	SUMMARY.	65
APPENDIX A.		66
APPENDIX B.		73
APPENDIX C.		77
APPENDIX D.		78
REFERENCES.		79
ACKNOWLEDGMENTS.		81

CHAPTER I

INTRODUCTION

In recent years communication system designers have begun to use the electromagnetic spectrum above 10 GHz in an effort to meet ever increasing bandwidth requirements. Overcrowding of the lower frequency bands have forced designers to make use of previously unused portions of the spectrum. Higher operating frequencies are also necessary to support extremely fast data rates which accompany recent advances in solid state technology.

At frequencies above 10 GHz, however, the effects of the earth's atmosphere upon communication signals dramatically increase. At these frequencies, a communications link designer must not only have a thorough knowledge of communication theory and systems design but must also have a working knowledge of electromagnetic wave propagation. The necessity for this additional qualification is evidenced by the literature. Until just recently, the effects of the clear atmosphere (no precipitation) on a communications signal were assumed to be negligible. However, it has been demonstrated[1] that clear air propagation effects can severely hamper a communications link under certain conditions. In fact, for signal scintillations whose minimum levels approach the system margin, the probability of an error in detection increases significantly.

Atmospheric effects upon a communications link can influence the amplitude, phase, angle-of-arrival, and polarization of the incident signal. These effects are manifest by amplitude and phase fluctuations, gain degradation, and depolarization. The causes of these effects include molecular absorption, scattering, refractive index inhomogeneities and atmospheric noise. These causes are not, in general, in one-to-one correspondence with the effects.

Molecular absorption at centimeter and millimeter wavelengths is primarily due to the presence of oxygen and water vapor. The former has a magnetic dipole moment, and the latter has an electric dipole moment.

Scattering and absorption in rain at these frequencies is pronounced because the dimensions of the hydrometers are on the order of or larger than the operating wavelength.

Refractive index irregularities arise from spatial and temporal variations in meteorological variables such as temperature, pressure, and water vapor content. These parameters are also influenced by wind velocity and direction.

In clear sky situations, atmospheric gas emission is the primary contributor to noise in this part of the spectrum.

The major purpose of studying the effects of the earth's atmosphere on electromagnetic waves at centimeter and millimeter wavelengths is to provide sufficient information for a communications link designer to most effectively use this portion of the spectrum. Increasing research in this area has introduced new applications and techniques.

In radio astronomy, for example, the effects of atmospheric propagation are important for several reasons. Earth-based radio astronomers must know what happens to a signal of extraterrestrial origin as it passes through the earth's atmosphere. Radio telescopes based outside the earth's atmosphere (such as those associated with Skylab) can use the knowledge obtained from the earth's atmosphere to study foreign planetary atmospheres and vice versa.

Recently, remote sensing has developed into a practical method, and in some situations the only method, of measuring meteorological variables at a distance. In particular, the structure constant of the refractive index and wind velocity perpendicular to the signal path can be calculated from statistics of a received signal.

One phase of experimental research on atmospheric propagation effects has been aimed at gathering long-term statistical data of a received signal. Statistics such as mean attenuation, fade distributions, and variance have been presented and analyzed in considerable detail. However, most of the analysis is performed in the time domain. The few papers that analyze the power density spectrum of the received signal estimate a slope and compare it with the theoretical value.

In this thesis, spectral characteristics of 2 and 30 GHz signals received from the Applications Technology Satellite-6 (ATS-6) are presented. These data were taken under clear air conditions. Second-order spectral characteristics such as slope and break frequencies are calculated at elevation angles ranging from 0.38 to 43.89 degrees. The dependence of the spectral characteristics on elevation angle is investigated.

CHAPTER II

THEORETICAL BACKGROUND

The earth's atmosphere is a random medium; therefore, wave propagation through the earth's atmosphere is a random process. As a result, literature dealing with this subject involves statistics of atmospheric parameters.

Centimeter and millimeter wave propagation is primarily affected by the troposphere. The ionosphere has little effect upon an electromagnetic wave at this frequency because the operating frequency is well above the plasma frequency.

The first successful theory of microwave propagation through atmospheric turbulence was that of Booker and Gordon[2]. Difficulties in their theory gave rise to the utilization of the statistical work of Kolmogoroff and Obukoff[3,4,5].

Modern theories of atmospheric turbulence have physical foundations in the dynamics of fluids. The basic picture is that of a blob of fluid, a turb, which is put into rotating motion by turbulent eddies. The turb dissipates its energy either by perturbing surrounding turbs, which creates smaller eddies, or by generating heat from frictional interaction with surrounding turbs.

Large volumes of the fluid containing large eddies are associated with significant kinetic energy whereas viscous frictional forces are thought to be small[6]. Thus, the spectrum of atmospheric turbulence, $\Phi(u)$, as a function of spatial wavenumber, u, is divided into three sections: (1) the energy subrange, (2) the inertial subrange, and (3) the dissipation subrange[7] (see Figure 1). The inner scale of turbulence, ℓ_i, is associated with the smallest eddy size, and the outer scale, ℓ_o, is associated with the largest eddy size. The inner and outer scales of turbulence are related to the spatial wave numbers, u_i and u_o, as $u_i = 2\pi/\ell_i$ and $u_o \cong 2\pi/\ell_o$. The inner scale of turbulence is on the order of 1 mm[8]. The outer scale of turbulence for an earth-space link can be taken as the effective height of the atmosphere since turbulent eddies larger than the effective height cannot exist. A value for the effective atmospheric height has been obtained by Devasirvatham and Hodge[1] as 6 km and will be used throughout this paper.

The shape of the turbulence spectrum is different in each of the three subranges. Most papers dealing with this subject assume that form of the turbulence spectrum which is applicable in the intertial subrange given by[9]

$$\Phi(u) = 0.033\, C_n^2\, u^{-m} \qquad (1)$$

where C_n^2 is the turbulence structure constant and m = -11/3 for the Kolmogoroff spectrum.

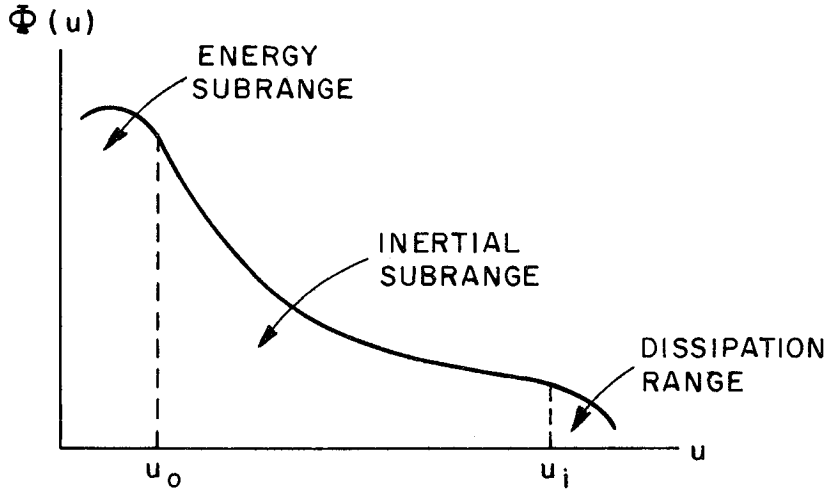

Figure 1. Spectrum of atmospheric turbulence.

The validity of this assumption is based upon the size of the first Fresnel zone with respect to the inner and outer scales of turbulence, i.e., upper and lower bounds are found such that $\ell_i << \sqrt{\lambda L} << \ell_o$,[8] where λ is the operating wavelength and L is the effective signal path length through the atmosphere.

Since propagation through the atmosphere is a random process, a signal received from a satellite is characterized in terms of covariance functions of the amplitude and phase scintillations. Expressions for the spectral density of the amplitude and phase scintillations are obtained by taking the Fourier transform of the covariance functions.

Analytical theories start with Maxwell's equations or the wave equation and introduce scattering and absorption characteristics to obtain differential equations from which the covariance functions can be calculated. The expressions obtained are quite difficult to evaluate which leads to various approximate methods. On the other hand, transport or radiative transfer theories deal directly with the transport of energy through a medium containing particles. The basic integrodifferential equation is known as the equation of transfer.

Among the various approximate methods used, the most common is the Rytov method. The Rytov method assumes that the sum of the perturbations on the wave are much less than the magnitude of the incident wave and that the dimensions of all refractive index perturbations are large compared to a wavelength. Lee and Harp[10] have shown that it is possible to relax these conditions by considering both the effects of these conditions on the mathematical expressions and the practical limitations of the measurement. Ishimaru[11] states that the Rytov solution is valid only when the variance of the log-amplitude fluctuation is less than $0.2 \sim 0.5$.

A commonly used approximation in the development of received signal covariance functions is Taylor's "frozen-in" hypothesis. Temporal variations in the received signal can be caused by refractive index changes along the signal path due to advection, convection, turbulent motions, etc. In addition, the motion of the atmosphere itself results in a transformation of spatial variations of refractive index into temporal variations. Taylor's hypothesis assumes that the temporal variations of the refractive index are only due to the average wind velocity perpendicular to the signal path and, thus, can be removed by a simple transformation of the spatial variation, i.e.,[8]

$$n(\bar{r},t) = n(\bar{r}-\bar{v}t) \tag{2}$$

where n is the refractive index, $\bar{r}$ is the position vector, $\bar{v}$ is the perpendicular wind velocity, and t is the temporal parameter. Thus, the effect of the frozen-in hypothesis on the time-lagged (temporal) amplitude covariance function, $B_x(\tau)$, can be expressed mathematically as

$$B_x(\tau) = \langle x(\bar{r},t)\ x(\bar{r},t+\tau)\rangle$$

$$= \langle x(\bar{r},t)\ x(\bar{r}-\bar{v}\tau,t)\rangle$$

$$B_x(\tau) = C_x(\bar{v}\tau) \tag{3}$$

where C_x is the spatial amplitude covariance function, τ is the time lag, x is the log amplitude fluctuation, and $\langle\ \rangle$ denotes ensemble average.

A quite significant assumption used in analyzing the amplitude fluctuations of the received signal is that of stationarity. The assumption of stationarity implies that the measurement is independent of the time it was taken. The validity of this assumption is tested in Chapter IV.

Mathematical Formulation of the Spectrum of the Amplitude Fluctuations

Using the Rytov method, it has been shown that[13] the received field can be expressed as

$$u(\bar{r},t) = u_0(\bar{r})\exp[\psi(\bar{r},t)] = u_0(\bar{r})\exp[x(\bar{r},t)+js(\bar{r},t)] \quad (4)$$

where $u_0(\bar{r})$ is the unperturbed incident field and the real part of ψ, x, is the log-amplitude fluctuation and the imaginary part of ψ, s, is the phase fluctuation.

The temporal amplitude covariance function is defined as

$$B_x(\tau) \triangleq \langle x(\bar{r},t)\ x(\bar{r},t+\tau)\rangle \quad (5)$$

where $\langle\ \rangle$ denotes ensemble average. Physically, $B_x(\tau)$ is a measure of the similarity of two observations of the log-amplitude fluctuations separated in time by τ seconds. If Taylor's hypothesis is assumed valid, the temporal amplitude covariance function is identical to the spatial covariance function (see Equation (3)).

Tatarskii[9] has shown that the spatial amplitude covariance function for a plane wave propagating in a medium with a purely real refractive index and a Kolmogoroff turbulence spectrum given in Equation (1) takes the form

$$B_x(\tau) = C_x(v\tau) = 2\pi \int_0^\infty F_x(u,L)J_0(uv\tau)u\,du \quad (6)$$

where

$$F_x(u,L) = \pi k^2 L \left[1 - \frac{k}{u^2 L}\ \sin\left(\frac{u^2 L}{k}\right)\right]\Phi(u)$$

and where $J_0(d)$ is the Bessel function of the first kind, v is the perpendicular wind velocity, L is the effective signal path length through the atmosphere, and k is the wave number ($k=2\pi/\lambda$).

The spectrum of the log-amplitude fluctuations is defined in terms of $B_x(\tau)$ as a Fourier transform relationship, i.e.,

$$W_x(f) = \int_{-\infty}^{\infty} B_x(\tau)e^{-j2\pi f\tau}\,d\tau \quad (7)$$

and since $B_x(\tau)$ and $W_x(f)$ are even

$$W_X(f) = 2 \int_0^\infty B_X(\tau) \cos(2\pi f\tau) d\tau \qquad (8)$$

Substituting (6) into (8) yields

$$W_X(f) = \frac{\pi}{4} \; 0.033 \; C_n^2 \; k^{7/6} \; \frac{L^{11/6}}{f_o}$$

$$x \int_0^\infty \left[1 - \frac{\sin(z+\Omega^2)}{(z+\Omega^2)}\right] (z+\Omega^2)^{-11/6} \exp\left[\frac{-(z+\Omega^2)}{D}\right] z^{-1/2} \, dz \qquad (9)$$

where

$$f_o = \frac{v}{\sqrt{2\pi\lambda L}}$$

$$z = \frac{u^2 L}{k}$$

$$\Omega = \frac{f}{f_o} = \sqrt{2\pi\lambda L} \; \frac{f}{v}$$

$$D = \left(\frac{5.91}{\ell_o}\right)^2 \frac{L}{k}$$

Note that k and λ are the operating wave number and wavelength, respectively, and are not related (directly) to the fluctuation frequency, f.

Assuming that D>>1 and changing the variable of integration to $x = z\Omega^{-2}$, Equation (9) becomes

$$W_X(f) = \frac{\pi}{4} \; 0.033 \; C_n^2 \; k^{7/6} \; L^{11/6} \; \frac{\Omega^{-8/3}}{f_o}$$

$$x \int_0^\infty \left[1 - \frac{\sin \Omega^2(x+1)}{\Omega^2(x+1)}\right] (x+1)^{-11/6} \; x^{-1/2} \, dx \qquad (10)$$

For small fluctuation frequencies $\Omega << 1$ and Equation (10) can be approximated as[9]

$$W_x(f) \overset{\Omega}{\sim} 0.075 \langle x^2 \rangle \frac{1}{f_o}, \quad \Omega \ll 1 \tag{11}$$

where $\langle x^2 \rangle = 0.077\, C_n^2\, k^{7/6}\, L^{11/6}$. For large fluctuation frequencies $\Omega \gg 1$ and Equation (10) is approximately

$$W_x(f) \overset{\Omega}{\sim} 0.57 \langle x^2 \rangle \frac{\Omega^{-8/3}}{f_o}$$

$$W_x(f) = 0.57 \langle x^2 \rangle f_o^{5/3} f^{-8/3}, \quad \Omega \gg 1 \tag{12}$$

Equations (11) and (12) intersect at a break frequency, f_{b2}, given by

$$f_{b2} = 2.14 f_o = \frac{2.14v}{\sqrt{2\pi\lambda L}} \tag{13}$$

Equation (13) provides a means for sensing the average wind velocity transverse to the signal path.

Figure 2 shows a Bode plot of $W_x(f)$ for a medium characterized by a real refractive index. Thus, in a medium with a purely real refractive index, the spectrum of the log-amplitude fluctuations is approximately flat up to f_{b2} and then rolls off as $f^{-8/3}$.

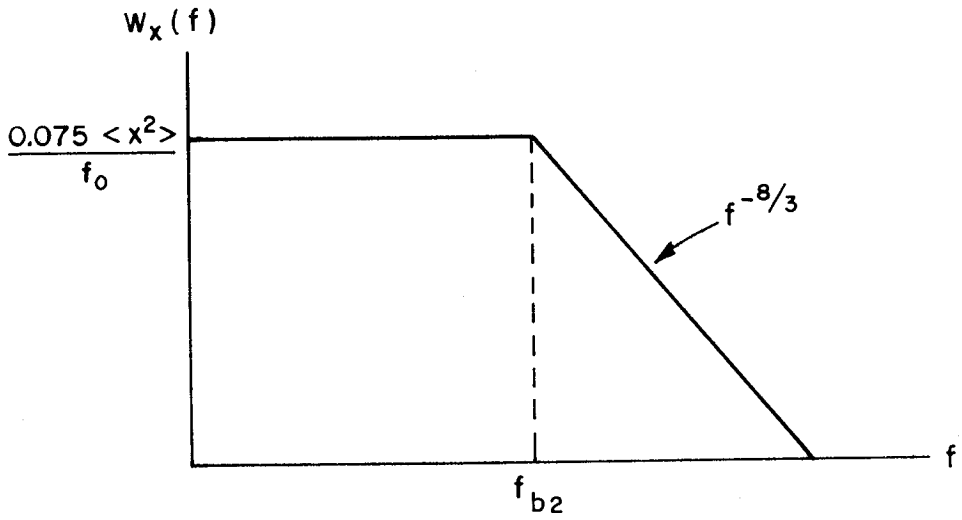

Figure 2. Theoretical spectrum of log-amplitude fluctuations in a medium characterized by a real refractive index.

Ott[14] has considered the spectrum of the log-amplitude fluctuations in a medium with a complex refractive index, n=a+jb. The spatial covariance function in this case is given by

$$C_x(v\tau) = 4\pi^2 k^2 \left|\frac{\partial n}{\partial T}\right|^2 L \int_0^\infty u\Phi_T(u) J_0(uv\tau)\,du \qquad (14)$$

where $\Phi_T(u) = 0.033\ C_T^2\ u^{-11/3}$ and C_T^2 is the structure constant of the temperature, T. The spectrum of the log-amplitude fluctuations in this case is found from Equation (7) for low f as

$$W_x(f) = 0.002598\ C_T^2\ k^2 \left(\frac{\partial b}{\partial T}\right)^2 L v^{5/3}\ f^{-8/3} \qquad (15)$$

and exhibits an $f^{-8/3}$ slope.

Comparing (11), (12), and (15) an intersection frequency between scattering and absorption regimes is found to be

$$f_{b1} = \frac{v}{2\pi}\left[0.1928 \left(\frac{\partial a/\partial T}{\partial b/\partial T}\right)^2 \frac{L}{k}\right]^{-3/8} \qquad (16)$$

Thus, the spectrum of the log-amplitude fluctuations can be separated into regions dominated by a scattering mechanism and an absorption mechanism. This modified spectrum is shown in Figure 3.

The validity of this mathematical model of the spectrum of the log-amplitude fluctuations will be investigated in Chapter V.

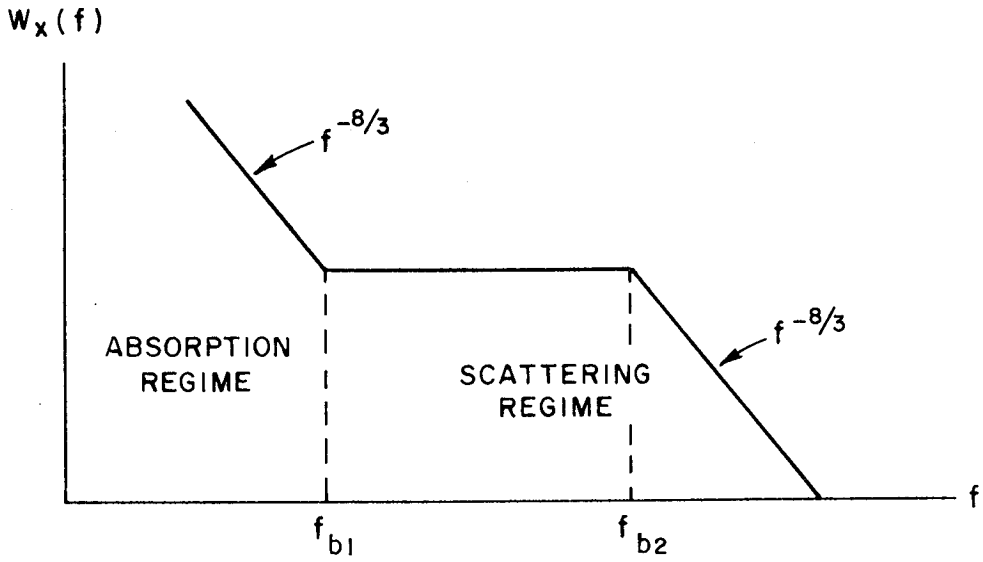

Figure 3. Spectrum of log-amplitude fluctuations in a medium characterized by a complex refractive index.

CHAPTER III

EXPERIMENT DESCRIPTION

The data presented in this thesis were obtained from the Applications Technology Satellite number 6 (ATS-6) during the time period extending from 28 August to 25 October, 1976. The purpose of the experiment was to investigate the propagation of millimeter waves through the atmosphere, specifically to determine the effect of elevation angle on various communication system parameters.

The receiving terminal was capable of measuring four frequencies: 30 GHz, 20 GHz, 2.075 GHz, and 360 MHz. However, the 20 GHz transmitter failed just prior to the experiment, and the 360 MHz data was unusable because of radio interference from local radio and television stations. Although only two frequencies were usable, their separation provided an excellent basis for data comparisons.

The ATS-6, a geosynchronous satellite, is used in some fifteen different experiments. Prior to the experiment reported herein, ATS-6 was located approximately 35^{o} East longitude over Lake Tanganika for the Satellite Instructional Television Experiment (SITE) based in India. In August, 1976, the satellite was moved to a position over the U. S. ($\sim 94^{o}$ West). This repositioning of the satellite provided an excellent opportunity for measuring the effect of elevation angle on propagation characteristics.

The satellite was moved an average of one degree per day and approximately one hour of data was taken at a number of different elevation angles except for the very low angles where almost continuous data were taken. The observable elevation angles ranged from -0.48 to 44 degrees; however, angles below 0.38 degrees were considered unusable because of the possibility of ground reflections.

The satellite's antenna for 30 GHz transmission is a 0.46 m parabolic reflector with linear polarization. The 2.075 GHz antenna is a 9.1 m parabolic reflector with right-hand circular polarization.

The receiving terminal is located at the Satellite Communications Facility of the Ohio State University's ElectroScience Laboratory (ESL), 1320 Kinnear Road, Columbus, Ohio (latitude: $40^{o}00'10"$N, longitude: $83^{o}02'30"$W). The facility along with the antennas used in the experiment are shown in Figure 4.

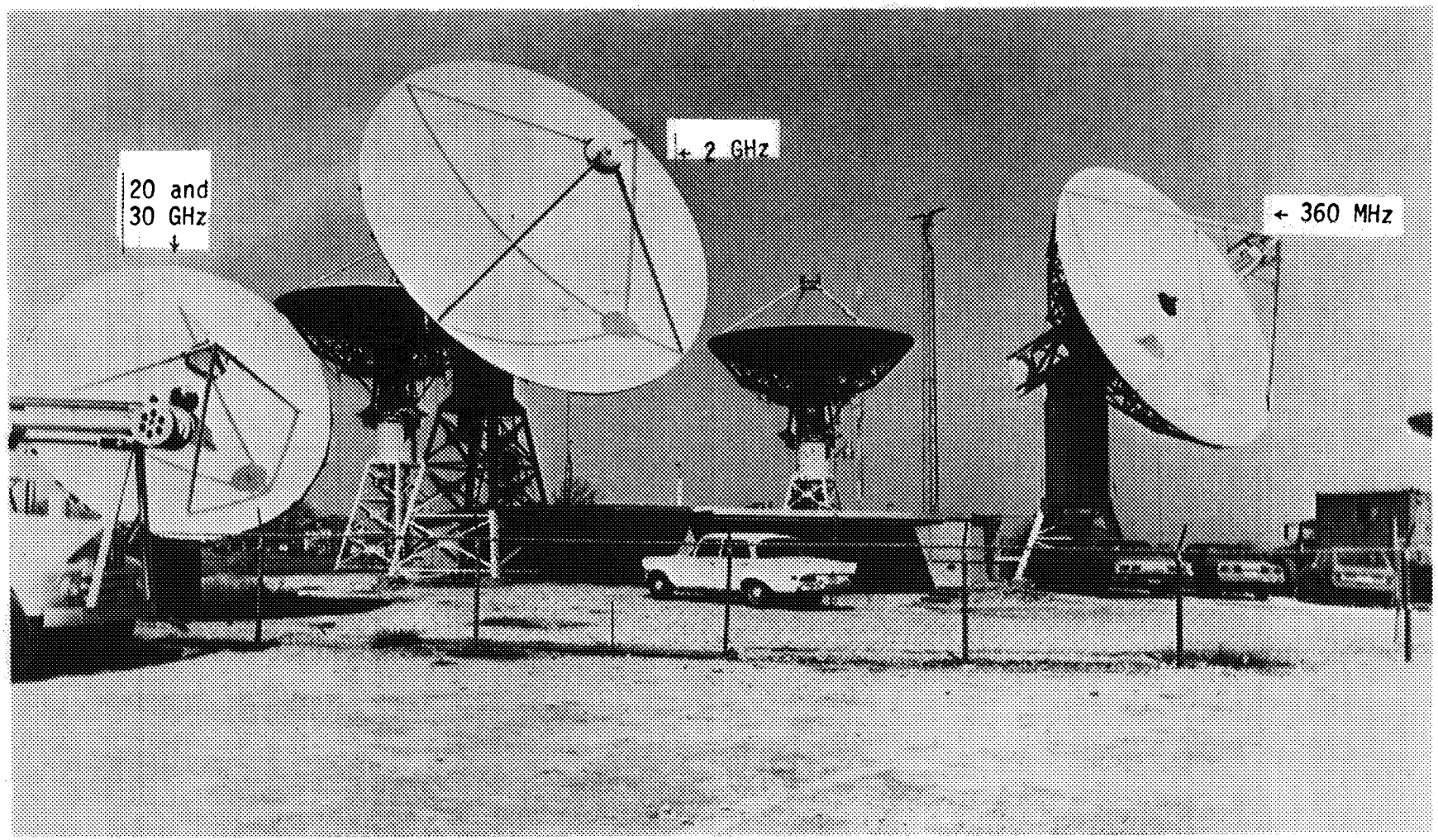

Figure 4. Satellite communications facility.

The 30 GHz receiver is shown in block diagram form in Figure 5. The antenna is a horn Cassegrainean-fed 4.6 m parabolic reflector with linear polarization. The beamwidth of this antenna at 30 GHz is 0.2 degrees. The front end (noise figure = 18 dB) consists of a solid state mixer and a stabilized local oscillator which produces a first intermediate frequency of 1.05 GHz. The front end is followed by a tunnel diode amplifier, manually-controlled step attenuators, and a Martin-Marietta phase-locked loop (PLL) receiver (modified for increased dynamic range). The receiver bandwidth is 55 Hz, and the signal-to-noise ratio averaged 52 dB at the higher elevation angles.

The 2.075 GHz receiver was built at the ElectroScience Laboratory, and the block diagram of it is shown in Figure 6. The antenna is a horn front-fed, 9.1 m parabolic reflector with linear polarization. The beamwidth at 2 GHz is 1.3 degrees. The front end (noise figure = 8.5 dB) consists of a transistor mixer and a stabilized klystron oscillator which produces a first IF of 30 MHz. The level of the 30 MHz IF was manually controlled by a step attenuator. The signal was then fed into the IF portion of a Collins 75S-3 receiver to produce a second IF of 455 KHz. The receiver bandwidth is 4.5 KHz, which made phase locking unnecessary. The 455 KHz signal was fed into a square-law detector. The average signal-to-noise ratio was approximately 52 dB.

The outputs of the receivers were recorded on strip charts and input to a digital data acquisition system.

Table I gives the link calculations for an elevation of 44 degrees.

Table I
Link calculations (elevation angle = 44^{o})

	2.075 GHz	30 GHz
Transmitter Power (dBm)	43.0	33.0
Spacecraft antenna gain (dB)	39.5	39.0
Spacecraft system loss (dB)	- 0.4	- 1.0
Free space path loss (dB)	-189.9	-213.4
Gas Losses (H_2O and O_2)(dB)	- 0.02	- 1.4
Ground antenna gain (dB)	40.0	57.8
Polarization loss (dB)	- 3.0	-
Ground waveguide loss (dB)	-	- 1.5
Signal level at front end (dBm)	- 70.8	- 89.0
Receiver noise temperature (^{o}K)	3800	18000
Receiver bandwidth (Hz)	4500	55
Receiver noise level (dBm)	-126.3	-138.7
Signal-to-noise ratio (dB)	55.5	51.2

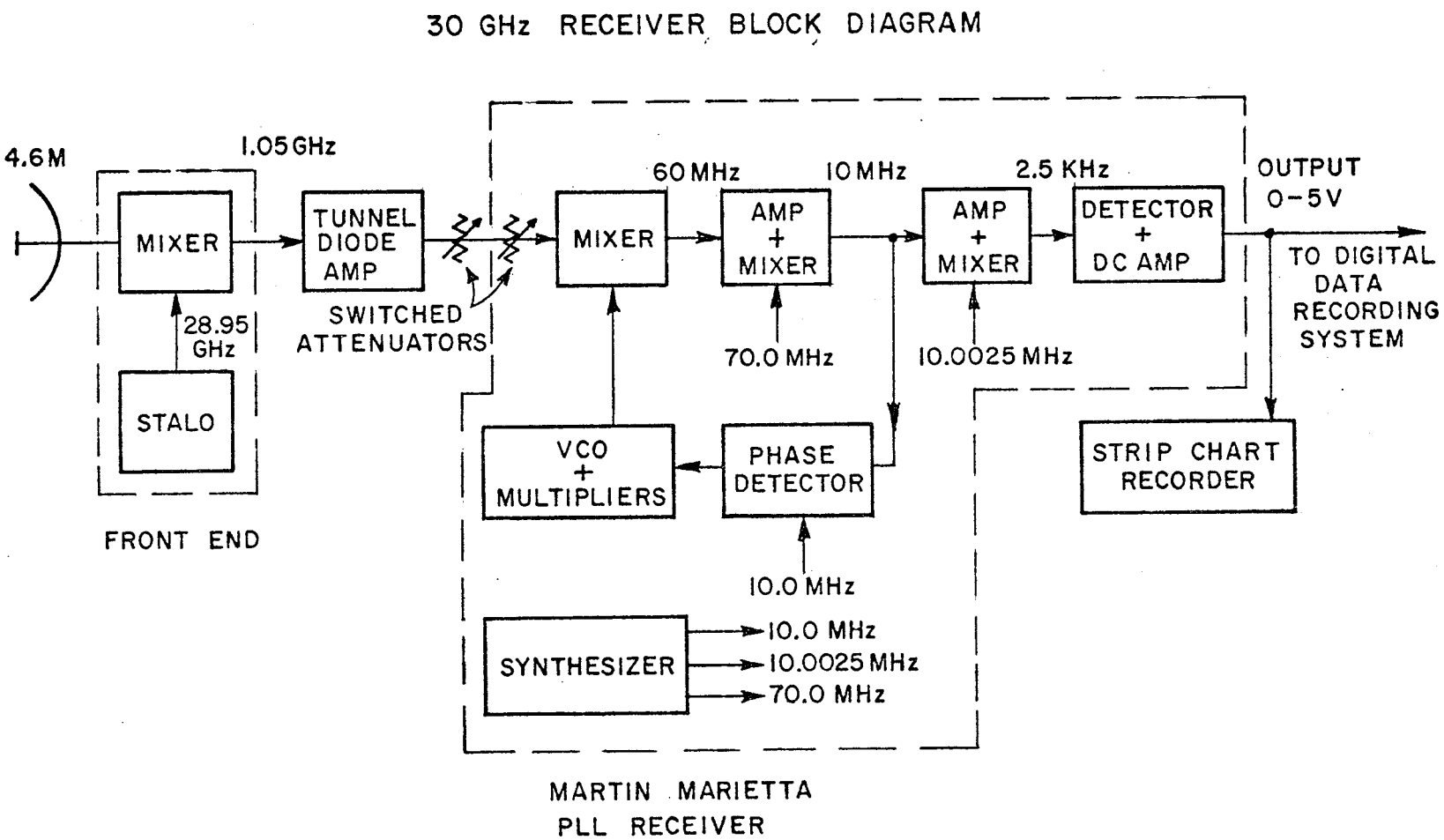

Figure 5. 30 GHz receiver block diagram.

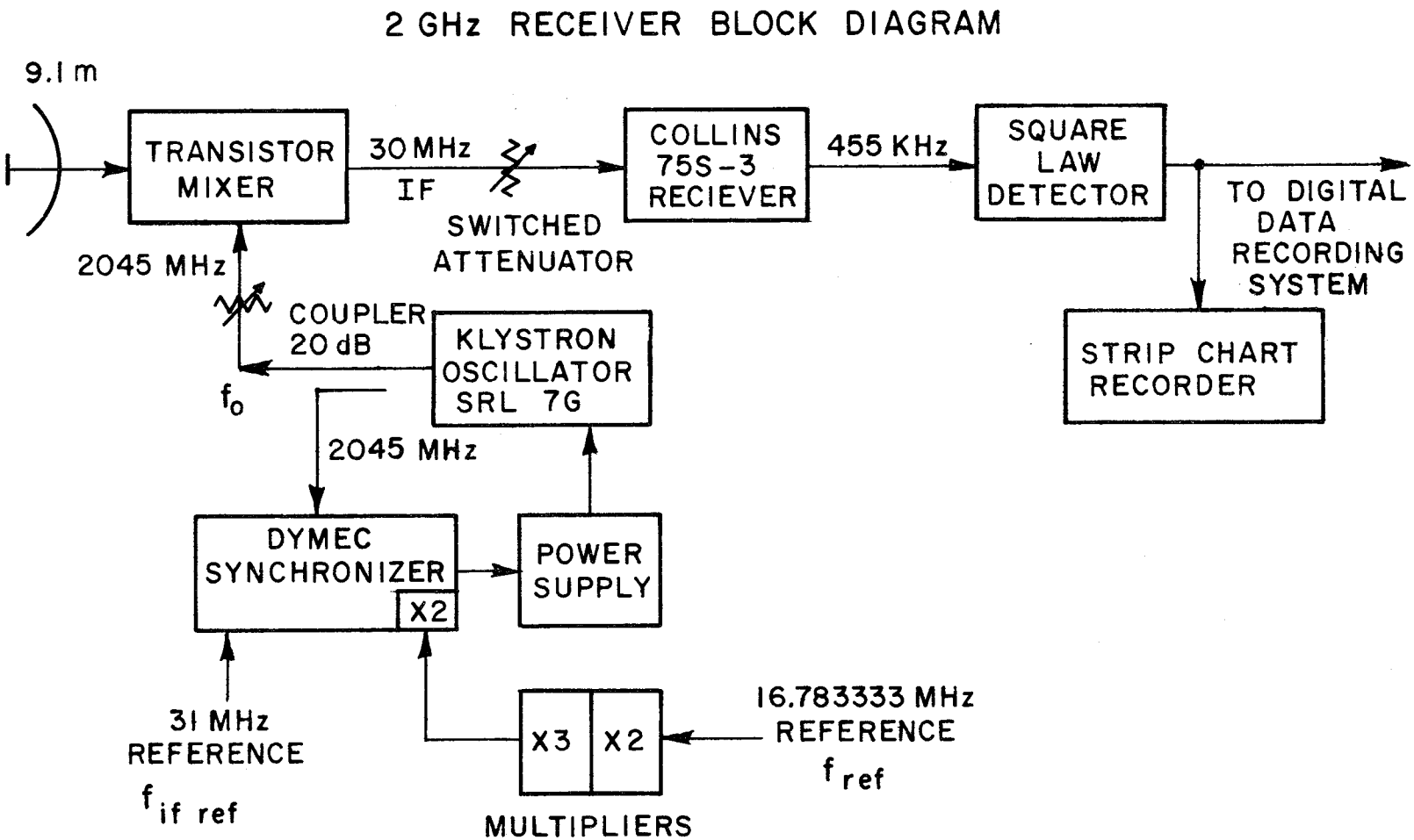

Figure 6. 2 GHz receiver block diagram.

The data acquisition system is shown in block diagram form in Figure 7. The output of the receivers ranged from 0 to 5 volts. These analog signal levels were multiplexed and fed into an 8 bit analog-to-digital converter (A/D). A controller for the A/D sampled the data at 10 samples per second and 200 samples per second. The 10 Hz rate was always used, while the 200 Hz rate was recorded for approximately five minutes at each elevation angle.

The main controller for the data acquisition system was an HP 2115A computer. It took care of sampling, formating, recording on 7 track magnetic tape, and keeping a log of operations such as attenuator settings, recording times, etc. The 7 track tapes were later converted to 9 tracks so that the data could be analyzed using the ESL Datacraft 6024 Computer.

The analog signal levels from each receiver and wind speeds were also recorded on strip charts.

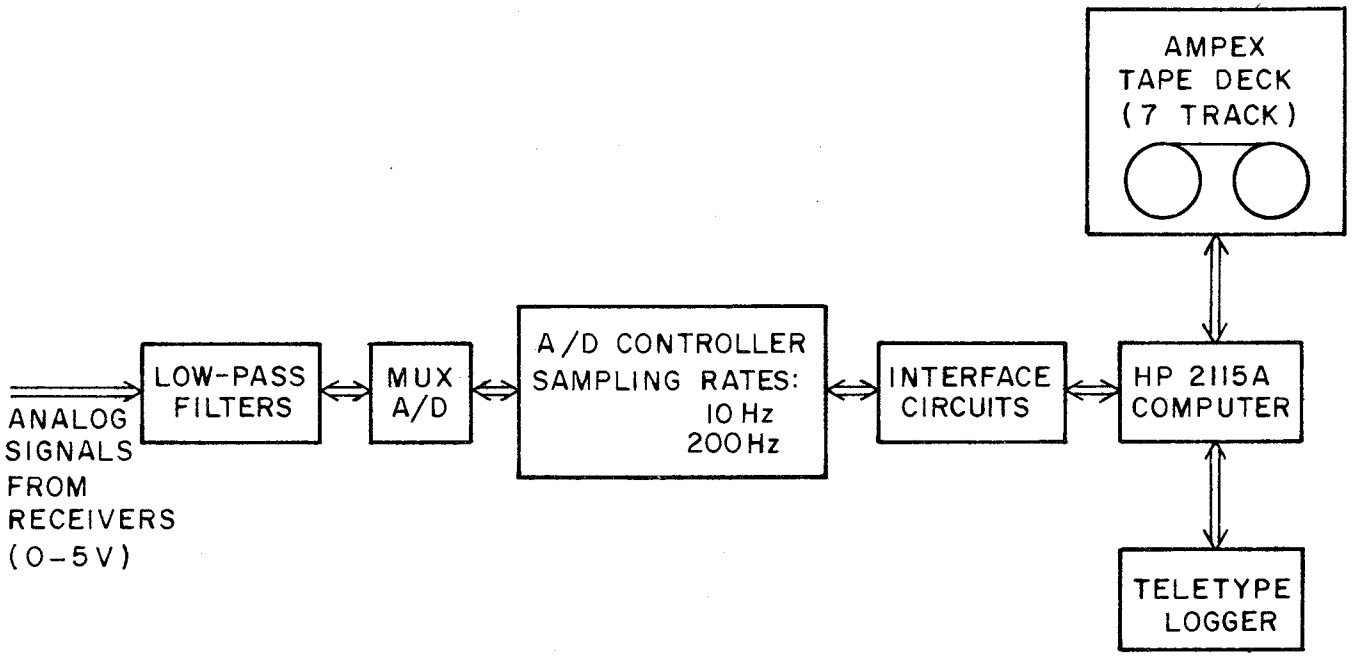

Figure 7. Digital data acquisition system.

CHAPTER IV

THE DATA

As mentioned previously, two sampling rates were used: 10 Hz and 200 Hz. However, the data taken at the 200 Hz rate were not used in the work that follows because spectral frequencies above 5 Hz were not significant and, thus, were for the most part contaminated by system noise (noise in the spectra is discussed in the last section of this chapter).

Figures 8 through 12 show some typical data samples at elevation angles of 0.38^{o}, 4.95^{o}, 18.11^{o}, 33.65^{o}, and 43.44^{o}. Each waveform shown consists of 2048 data points taken at the 10 Hz sampling rate (1 data record = 2048 data points). There is obviously a significant effect of elevation angle on the received signals. This effect has been studied in the time domain by Devasirvatham and Hodge[1]. In this study, the effect of elevation angle on the signal spectra is considered.

A. Stationarity

If the signal is "wide sense stationary"[15] its mean, m, is independent of time and its autocorrelation function, $R(\tau)$, is dependent only on lag time, τ, i.e., it is not dependent on absolute time. In analyzing a data record, the mean of all 2048 points was calculated; thus, the mean is forced to be independent of time for any given data record (compensation processing for a nonstationary mean is discussed in the next section).

The autocorrelation function is defined in general as[21]

$$R(\tau) = \lim_{T\to\infty} \frac{1}{2T} \int_{-T}^{T} f(t)f(t+\tau)dt \qquad (17)$$

It is more convenient, however, to calculate an autocovariance coefficient which is related to the signal waveform, f(t), by

$$\rho(\tau) = \lim_{T\to\infty} \frac{1}{2T} \int_{-T}^{T} \frac{[f(t)-m][f(t+\tau)-m]dt}{\sigma^2} \qquad (18)$$

where m is the mean and σ the standard deviation. For a periodic, sampled waveform, Equation (18) can be approximated as

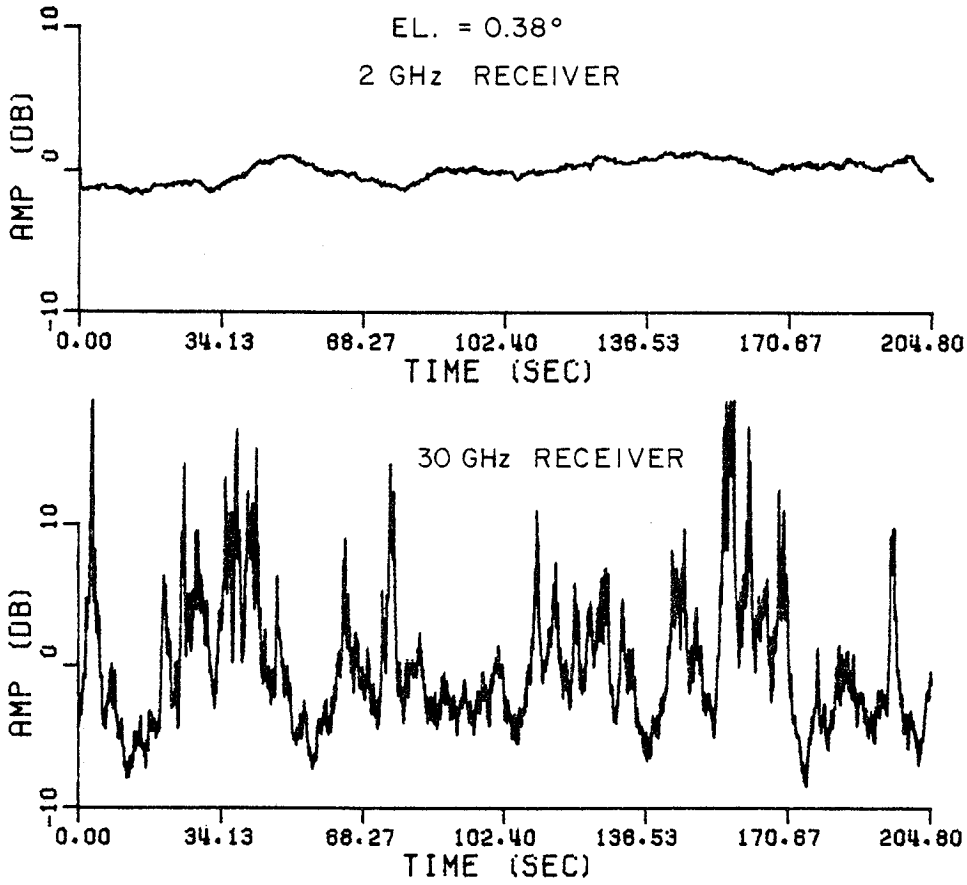

Figure 8. Received signals at el. = 0.38^{o}.

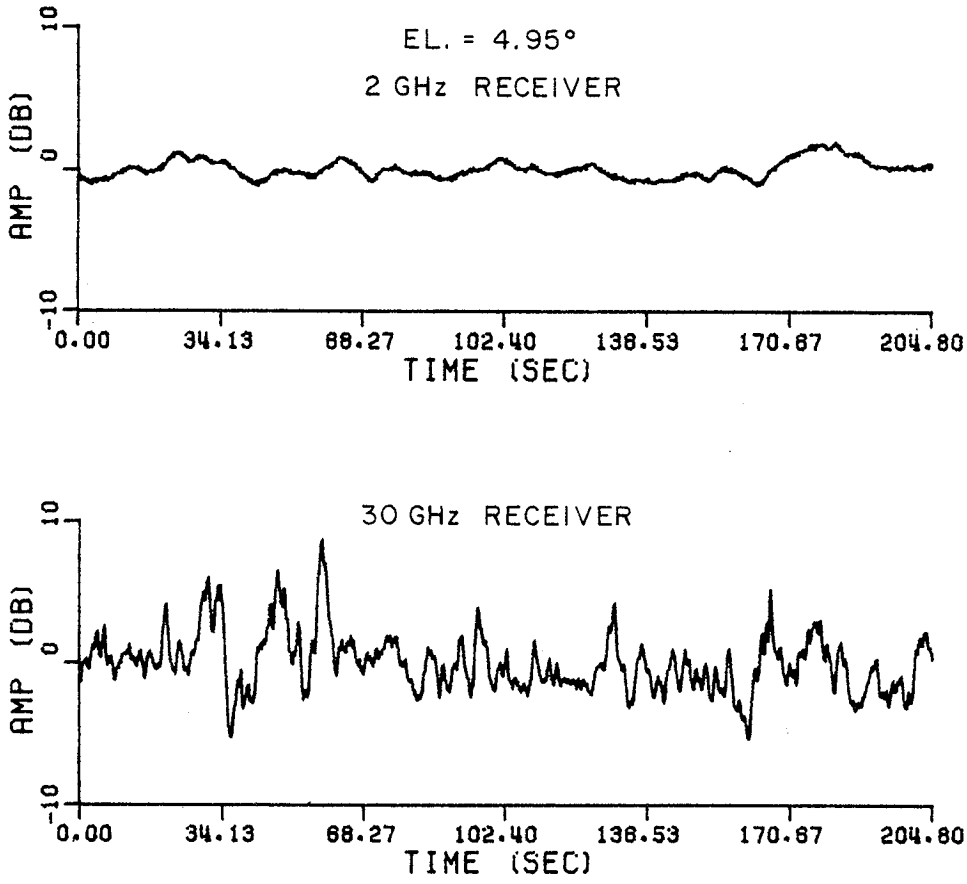

Figure 9. Received signals at el. = 4.95^{o}.

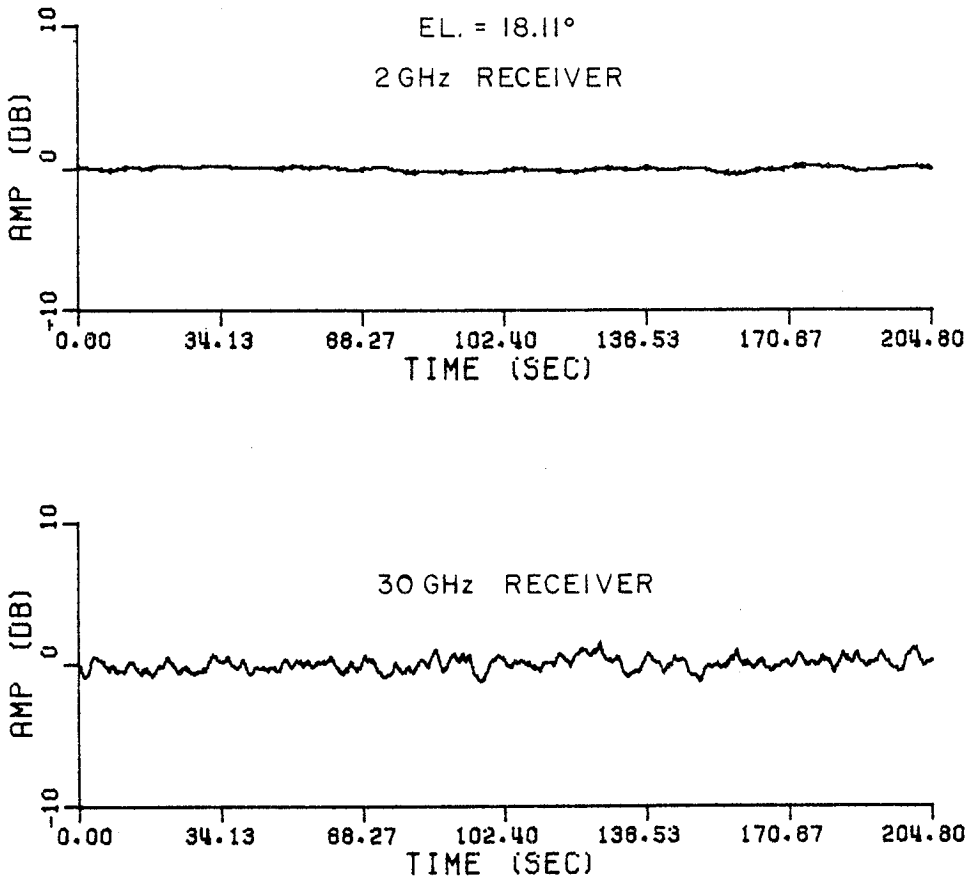

Figure 10. Received signals at el. = 18.11^{o}.

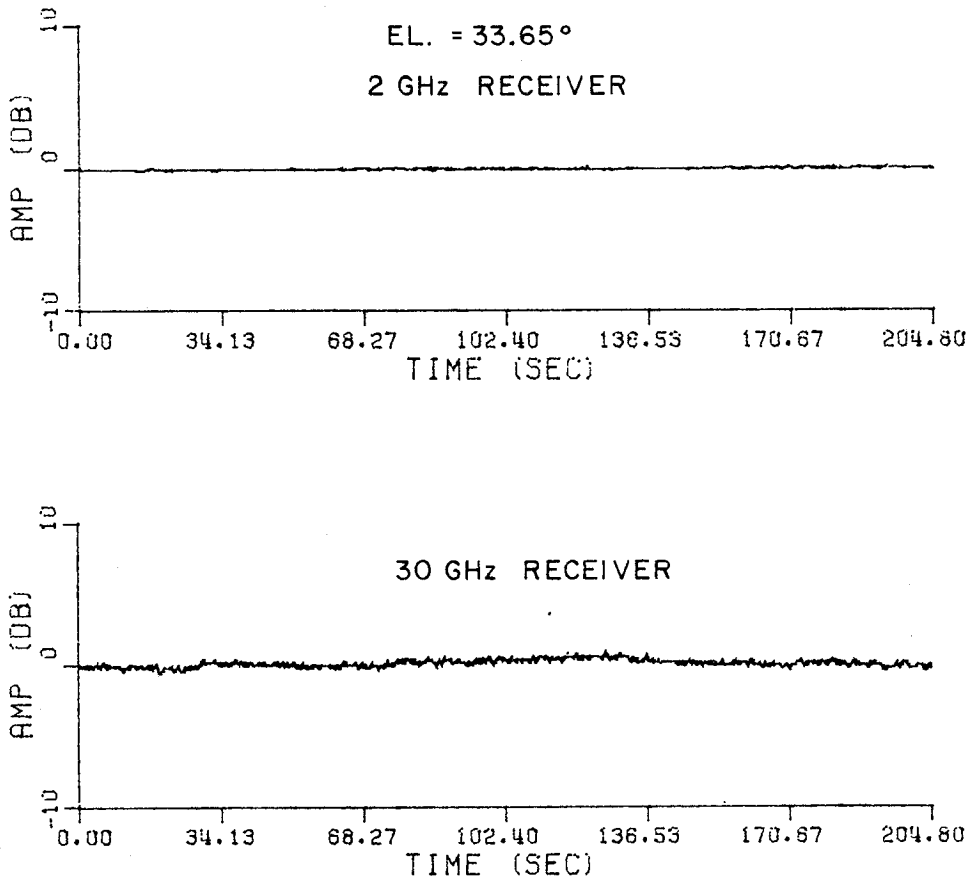

Figure 11. Received signals at el. = 33.65°.

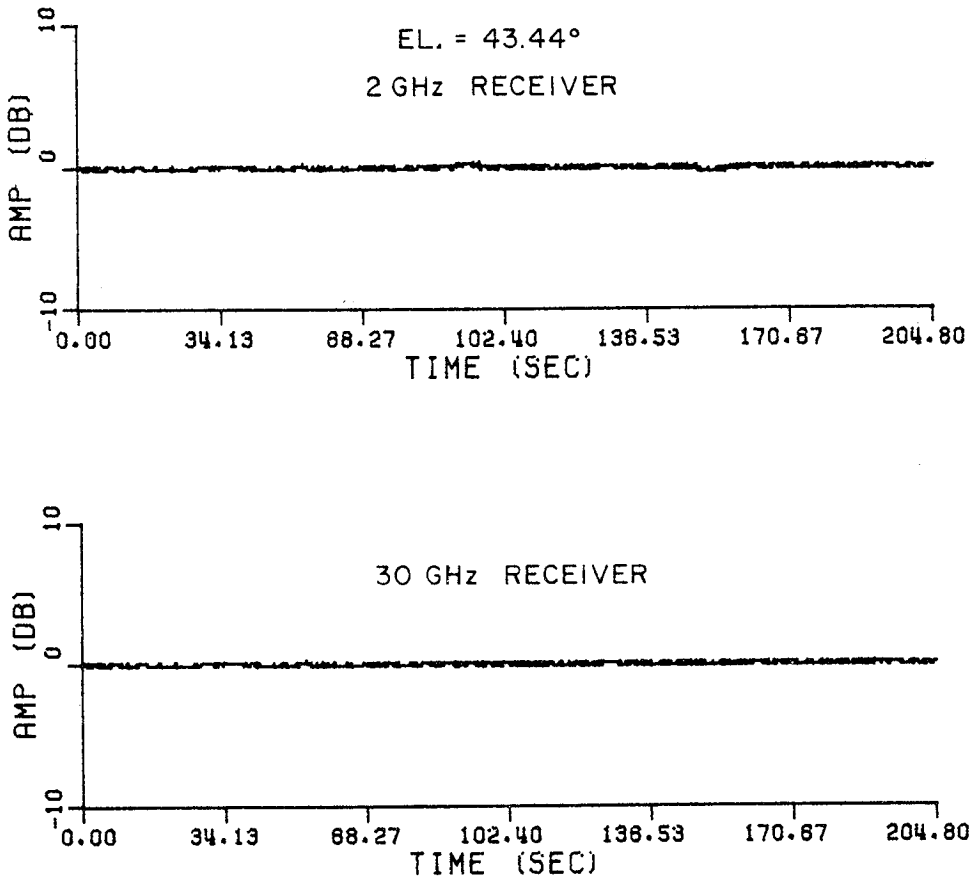

Figure 12. Received signals at el. = 43.44^{o}.

$$\rho(\tau_{ij}) \cong \frac{1}{N} \sum_{i=1}^{N} \frac{[f(t_i)-m][f(t_{i+j})-m]}{\sigma^2} \tag{19}$$

with increasing accuracy as $N \to \infty$.

If the autocorrelation function is dependent only on lag time then the time interval that is to be examined for stationarity can be divided into sections and the similarity of the autocorrelation function, and similarly the autocovariance coefficient, will determine the relative stationarity of the waveform.

The data samples shown in Figures 8-12 were examined for stationarity using the method described above. An additional 2048 samples immediately following the samples shown in Figures 8-12 were used so that the signal stationarity could be examined over the length of one data record. The first 2048 samples will be referred to as the left half and the second 2048 samples will be referred to as the right half. The autocovariance coefficients were calculated for both halves at each of the five sample elevation angles and are shown in Figures 13-17. For a numerical comparison, the squared differences between the left and right halves were defined as

$$\text{Squared Difference} = 10 \log_{10} \frac{\sum_{i=1}^{N} [\rho_L(t_i) - \rho_R(t_i)]^2}{\frac{1}{2} \sum_{i=1}^{N} [\rho_L^2(t_i) + \rho_R^2(t_i)]} \text{ (dB)} \tag{20}$$

where ρ_L is the autocovariance coefficient function for the first 2048 points and ρ_R is the autocovariance coefficient for the second 2048 points.

The squared differences for each of the five samples are shown in Table II along with the signal variances. Note that the stationarity of the sampled waveform improves steadily with increasing elevation angle. The nonstationarity at low elevation angles is probably due to large signal variances caused by strong fluctuations; as mentioned in Chapter II, signal (log-amplitude) variances greater than 0.2 to 0.5 are considered to be caused by strong fluctuations. The signal variances are shown in Figure 16 as a function of elevation angle^{-1}. The curves represent regressive fits of the data to a spherical-earth model for the signal path length. Ishimaru's strong fluctuation criterion corresponds to -7 dB in Figure 16. Thus, only the 30 GHz data under 4^0 elevation angle is in the strong fluctuation regime according to this criterion.

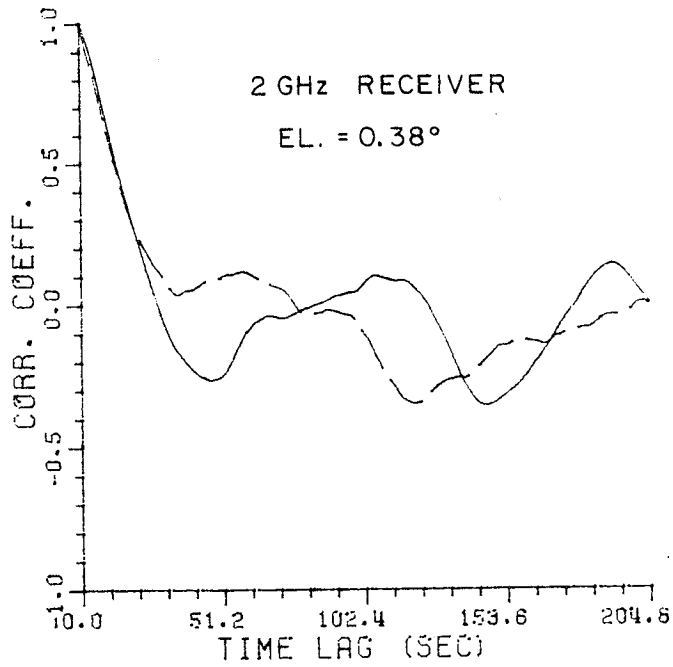

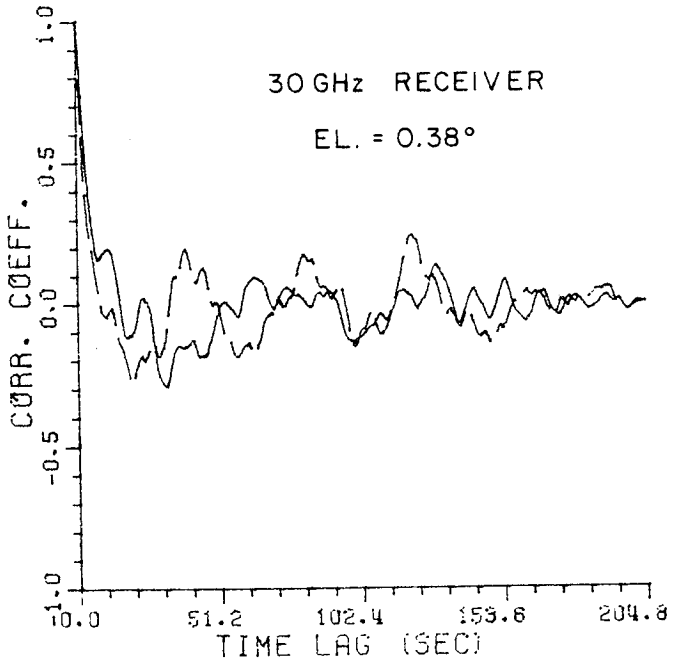

Figure 13. Correlation between two consecutive data records at el. = 0.38°.

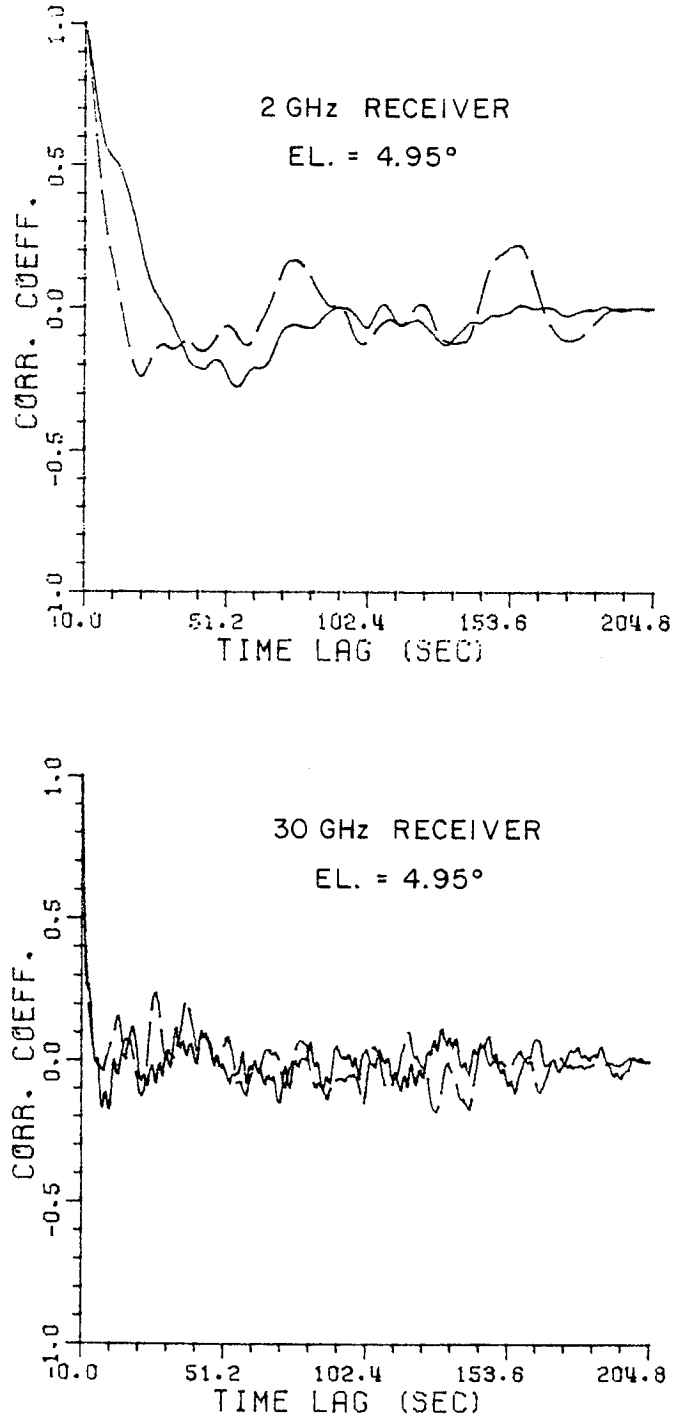

Figure 14. Correlation between two consecutive data records at el. = 4.95°.

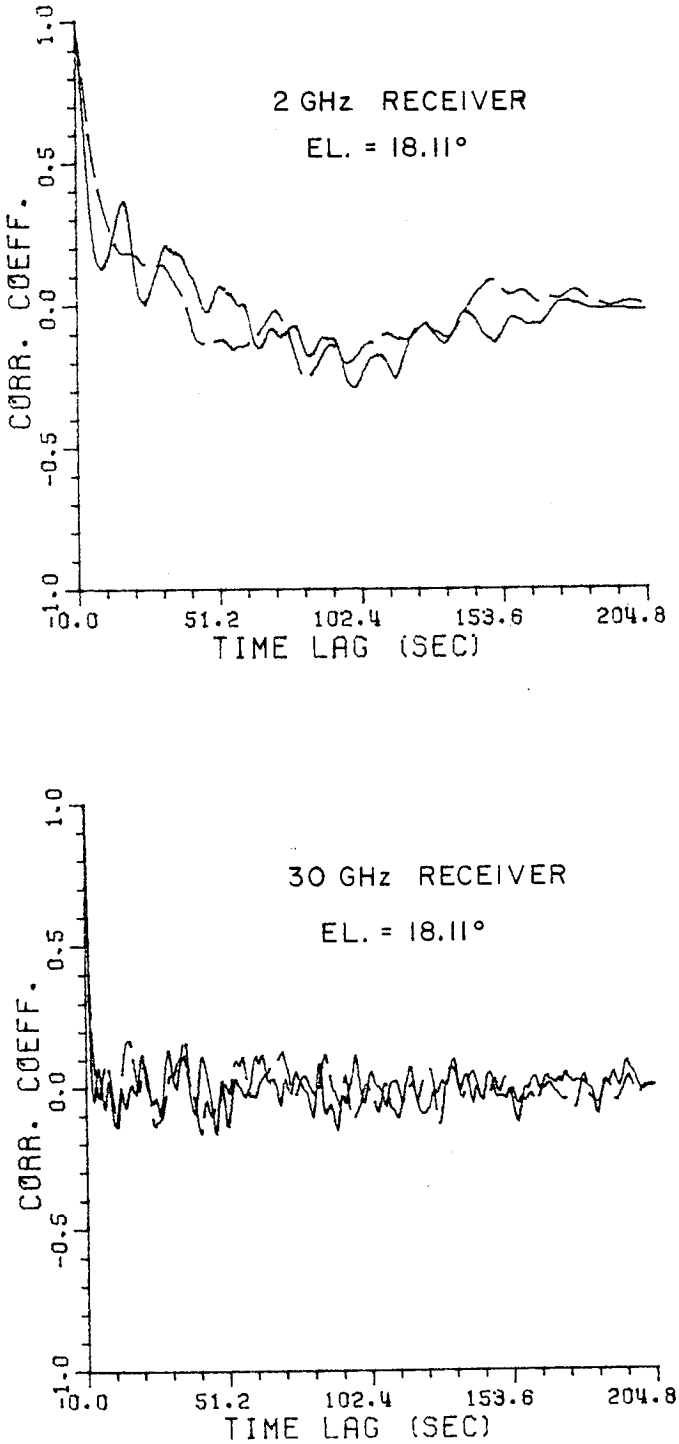

Figure 15. Correlation between two consecutive data records at el. = 18.11°.

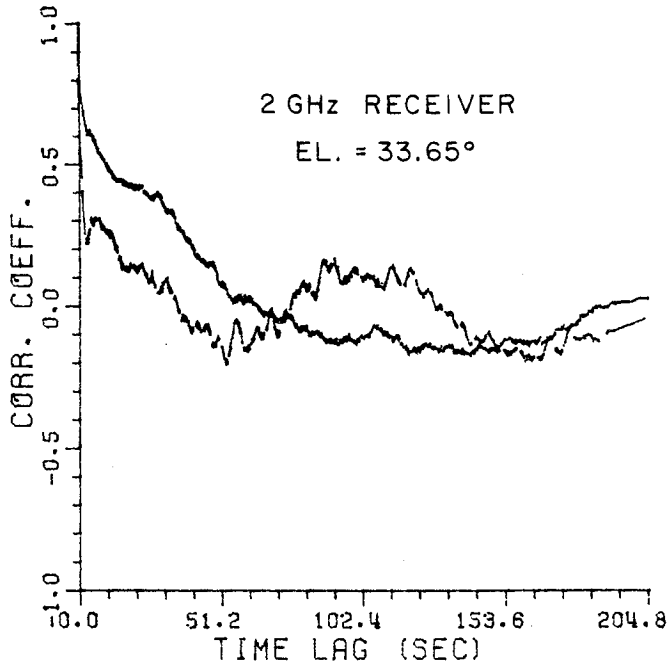

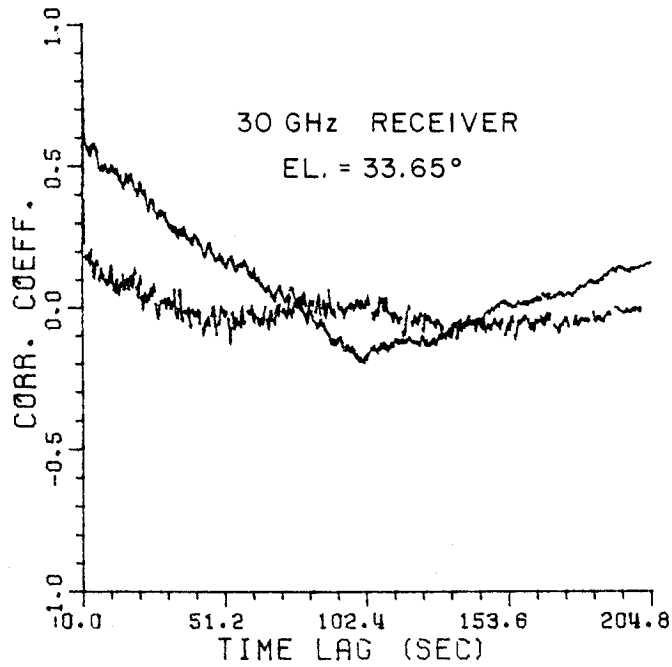

Figure 16. Correlation between two consecutive data records at el. = 33.65°.

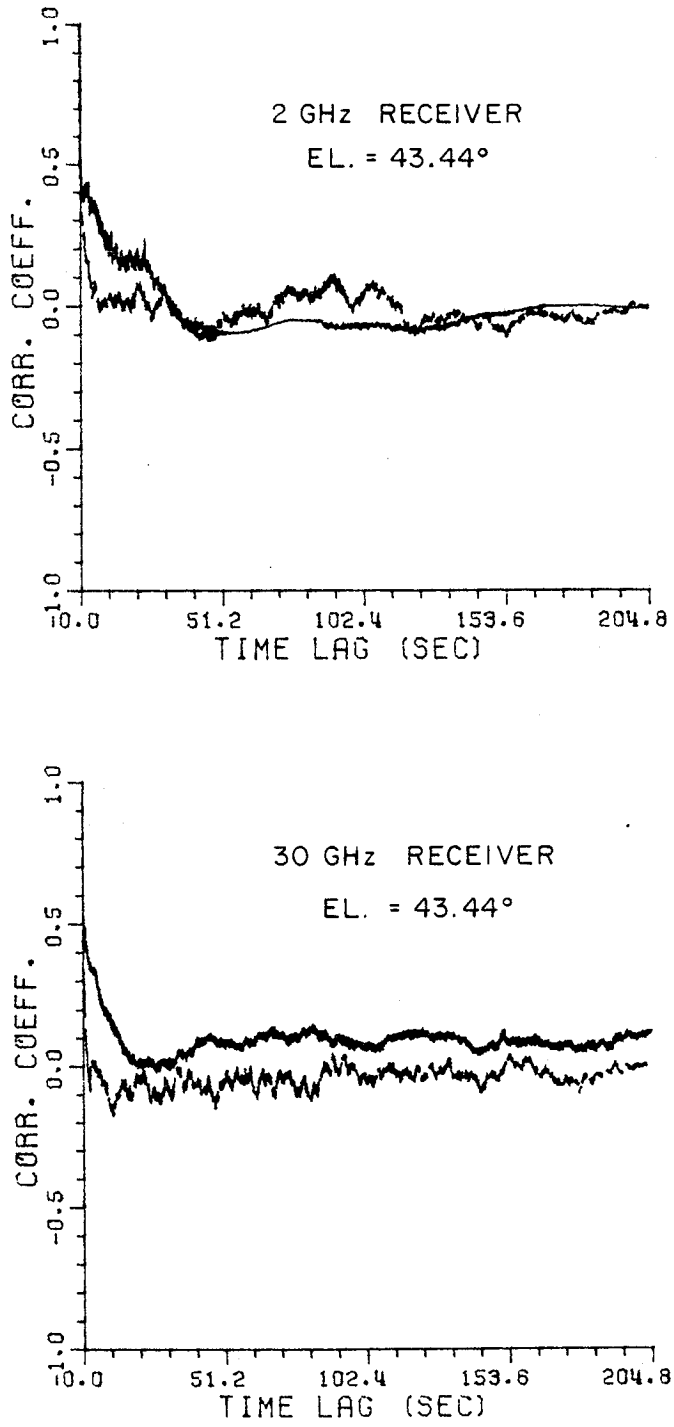

Fiugre 17. Correlation between two consecutive data records at el. = 43.44°.

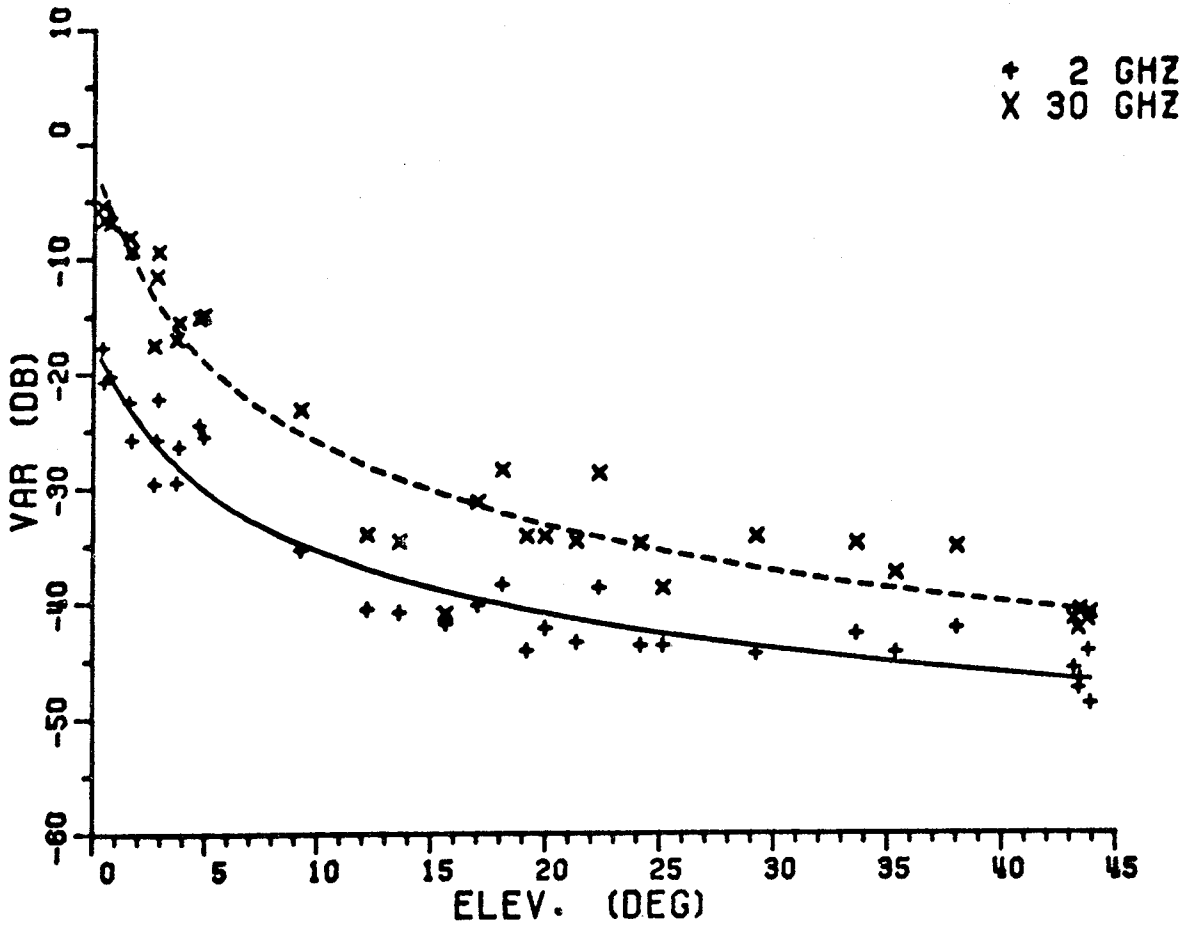

Figure 18. Mean amplitude variance with elevation angle (spherical earth model). Variance is normalized to d.c. power levels.

Table II
Autocovariance coefficient comparison

2 GHz Receiver		
El. (deg)	Mean signal amplitude variance (dB)	Squared difference (dB)
0.38	-17.5	-14.3
4.95	-25.5	-18.6
18.11	-37.0	-32.6
33.65	-42.0	-38.7
43.44	-43.0	-42.6

30 GHz Receiver

0.38	- 5.5	- 6.1
4.95	-15.0	-10.7
18.11	-28.0	-22.5
33.65	-33.0	-30.3
43.44	-40.0	-35.2

All of the correlation coefficients tend toward zero with increasing lag time except for the right halves at el. = 33.65^{o} and 43.44^{o}. Their behavior is probably caused by short periods of no bit changes in the sampled waveform.

B. Processing Techniques

A Fast Fourier Transform (FFT) technique was used to approximate the power density spectrum of the sampled signals (the FFT actually produces a periodigram). The periodigram was produced in two steps: (1) the FFT was used to obtain the Fourier Transform and its conjugate, $F(\omega)$ and $F^*(\omega)$, from the time-domain waveform, $f(t)$†; (2) then the conjugate pairs were multiplied and normalized by the d.c. component of the power. (The spectral components were normalized to the power in the d.c. component rather than the mean power so that the dependence of the spectral slope on variance was not removed.) The result, $S(\omega)$, was a periodigram which approximates the power density spectrum with increasing accuracy as the sampling rate increases. This two-step process is shown schematically in Figure 19.

†Note that $f(t)$ is in units of volts; thus, $f(t)$ represents the amplitude fluctuation and not the log-amplitude fluctuations. However, the amplitude fluctuations and the log-amplitude fluctuations are similar if the fluctuations are small.

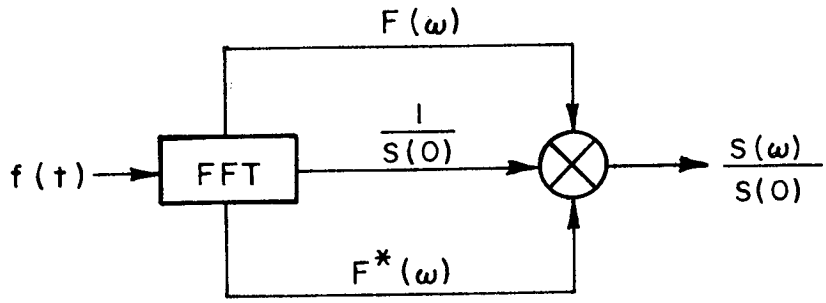

Figure 19. Generation of a periodigram.

The highest spectral component that can be produced is the folding frequency, f_H, which is half the sampling frequency, f_s, i.e., $f_H = f_s/2$.

The lowest component is determined by the number of data points, N, and is found from the relation $f_L = (f_s/2)/(N/2) = f_s/N$. For example, a periodigram produced from data sampled at a rate of 10 Hz which uses 2048 points will contain spectral components at $f_n = nf_s/N = 0.00488n$ Hz, where n=1,2,3,...,1024. Periodigrams produced from the typical samples are shown in Figures 20-24.

Two time-domain processing techniques were used to make the periodigram produced by the FFT more accurately approximate the true power density spectrum of the received signal: (1) slope compensation and (2) cosine tapering. The purpose of slope compensation is to remove sloping trends of the mean signal level. The effect of slope compensation on the periodigrams is that of reducing aliasing and Gibb's phenomena. Cosine tapering is a windowing technique the purpose of which is to reduce sidelobe levels in the spectrum.

Slope Compensation Algorithm

Sloping trends in the mean signal level are compensated by first considering M points (M=100 for results that follow) on each end of the sampled waveform, see Figure 25. Averages of these end samples are calculated, m_1 and m_2, and a straight line is drawn through these averages from P_{m1} to P_{m2}. Each sample point is then level adjusted according to the offset level of the line through P_{m1} and P_{m2}. The slope compensation subroutine is given in Appendix A.

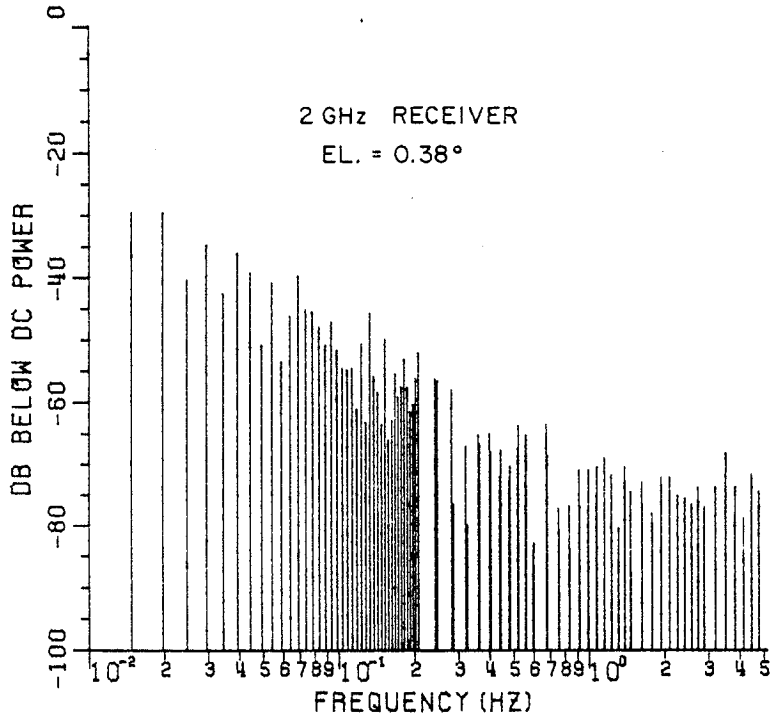

(a)

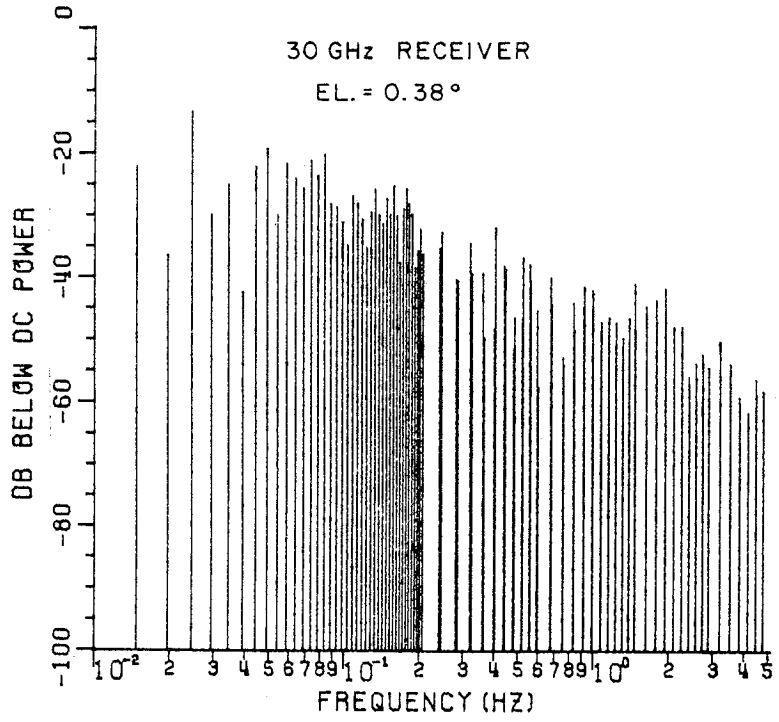

(b)

Figure 20. Periodigram of sampled waveform at el. = 0.38^{o}.

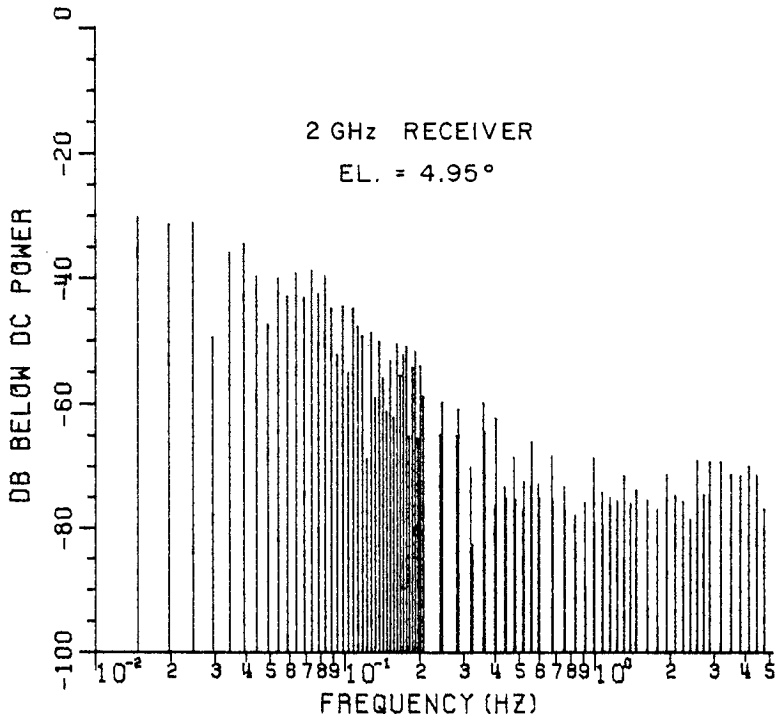

(a)

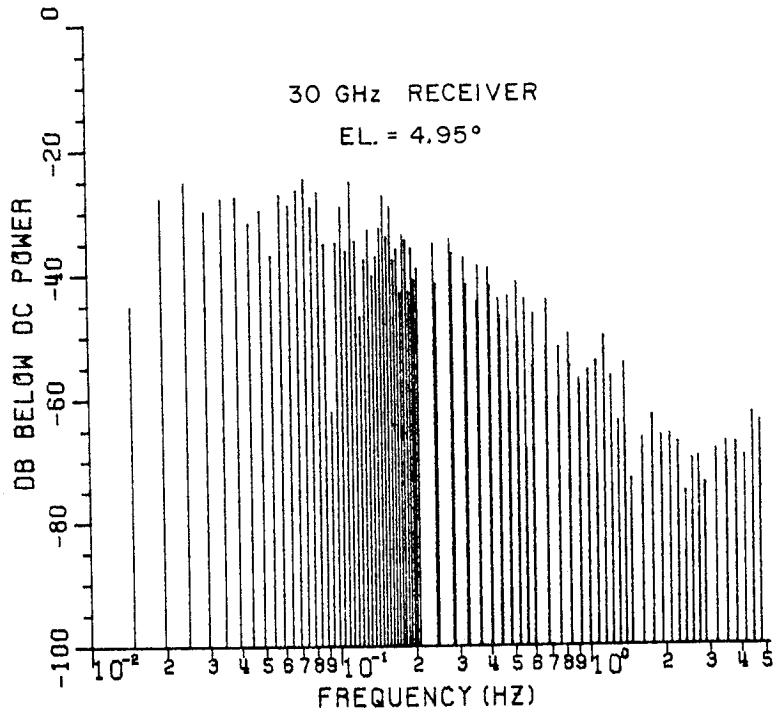

(b)

Figure 21. Periodigram of sampled waveform at el. = 4.95°.

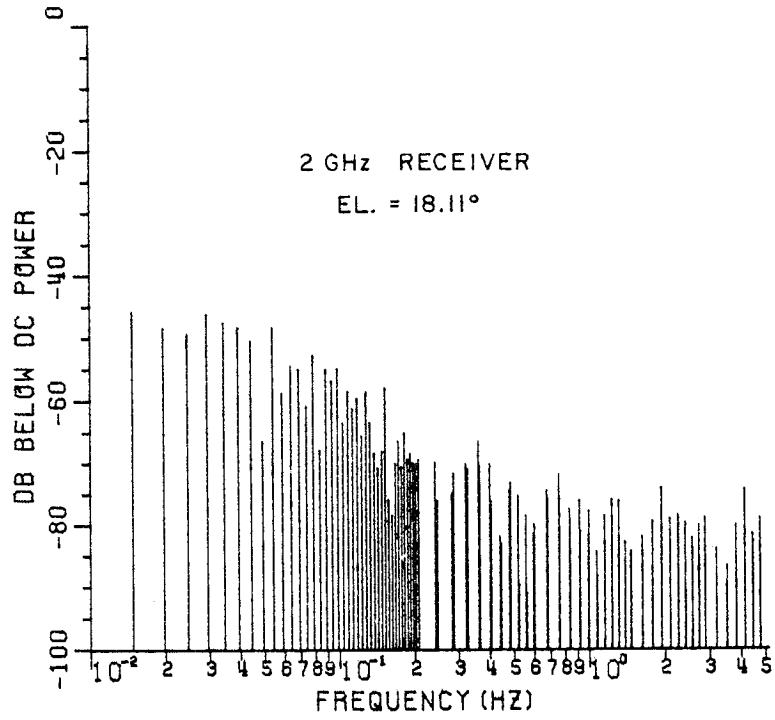

(a)

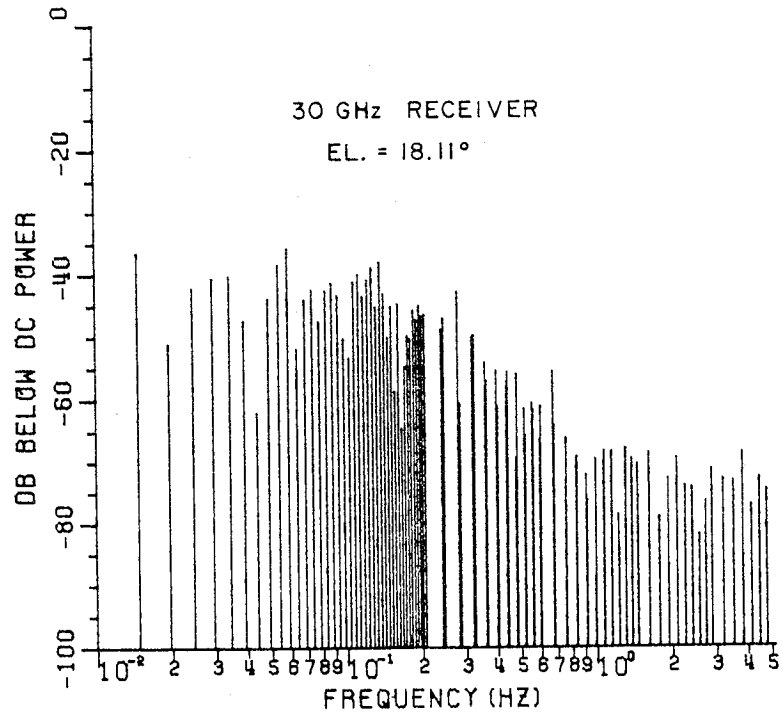

(b)

Figure 22. Periodigram of sampled waveform at el. = 18.11°.

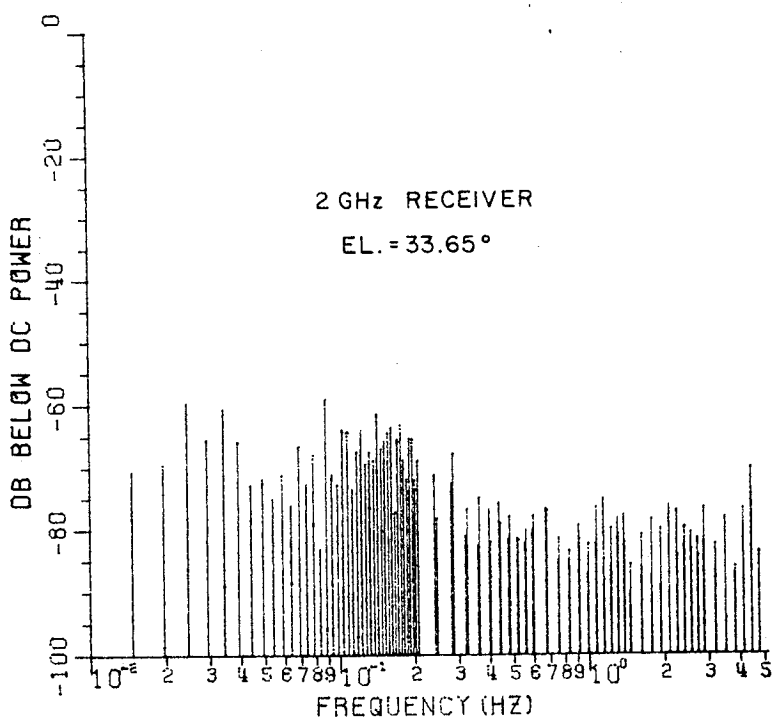

(a)

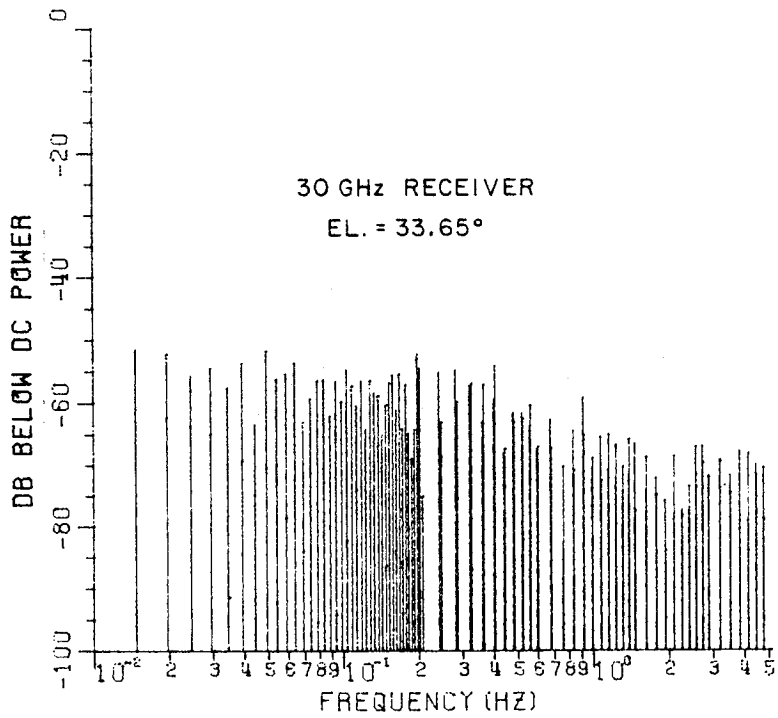

(b)

Figure 23. Periodigram of sampled waveform at el. = 33.65°.

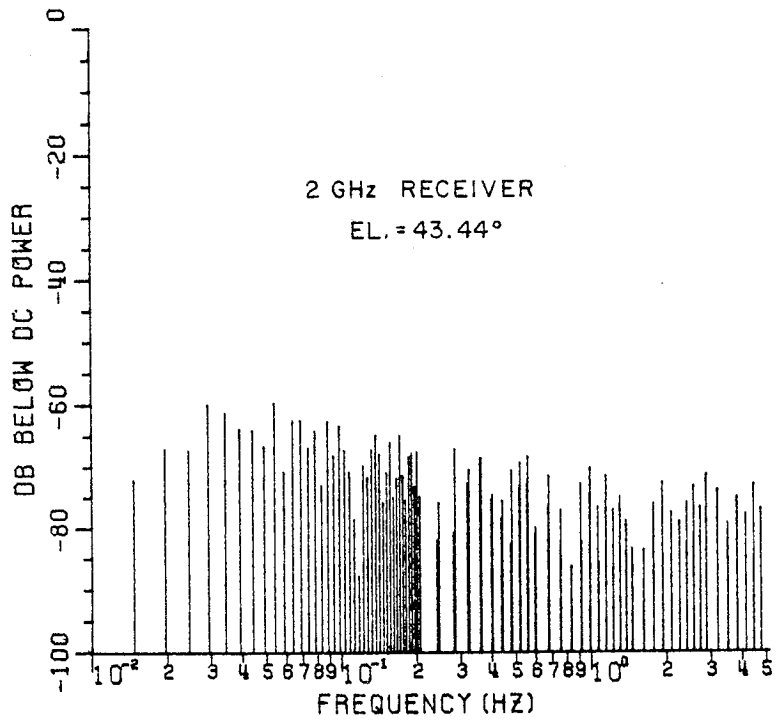

(a)

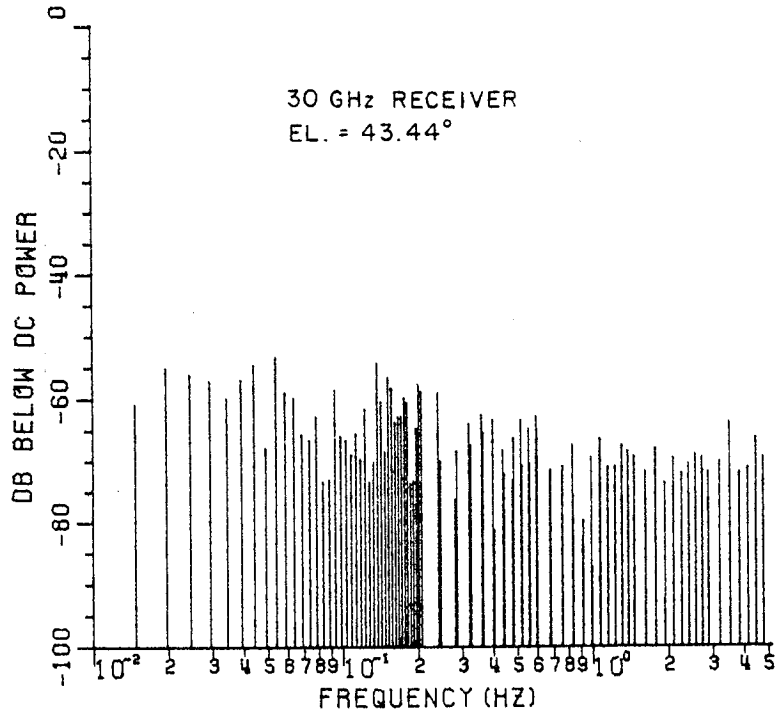

(b)

Figure 24. Periodigram of sampled waveform at el. = 43.44°.

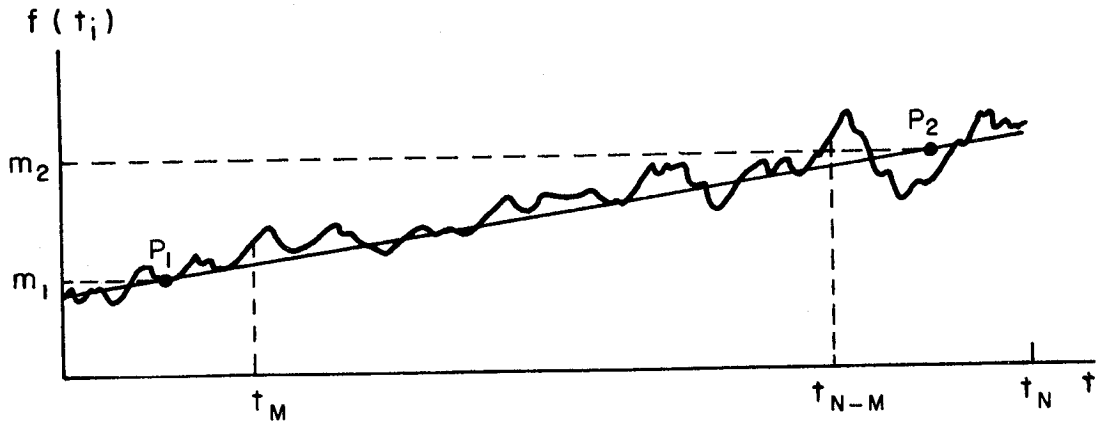

Figure 25. Slope compensation configuration.

Cosine Taper Algorithm

The window function, $f_{CT}(t)$, for the cosine taper is given by[16]

$$f_{CT}(t) = \frac{1}{2}\left(1 + \cos\frac{\pi t}{T}\right) f_{SAMP}(t),\ T \leq t \leq T \tag{21}$$

or in discrete form as

$$f_{CT}(t_i) = \frac{1}{2}\left[1 + \cos\pi\ \frac{(M-i)}{M}\right]\ f_{SAMP}(t_i),\ i=0,1,2,\ldots,M \tag{22}$$

where t_i is the time corresponding to the ith sample point and M is the number of points to be tapered on each end of the waveform (the value of M was chosen as 20). The cosine taper subroutine is given in Appendix A.

If $f_{SAMP}(t)$ is a pulse of width 2T then the Fourier transform of $f_{CT}(t)$ is

$$F_{CT}(\omega) = \frac{\pi \sin T\omega}{\omega(\pi^2 - T^2\omega^2)} \tag{23}$$

Note that $F_{CT}(\omega)$ is proportional to ω^{-3} as $\omega \to \infty$.

Figure 26 shows periodigrams produced from each of these processing techniques. In analyzing the data, both processing techniques were used to produce periodigrams; however, only 40 points (20 points on each end of a 2048-point data sample) were tapered.

A third processing technique, filter compensation, was performed in the frequency domain. Referring to Figure 7 in Chapter III, note that the signals are low-pass-filtered before they are sampled. To compensate for the roll-off of this filter, each spectral component in a periodigram is increased by a value determined by the characteristic curve of the filter. Figure 27 shows the 30 GHz filter characteristic curve and the effect of filter compensation on the spectral components. The effect of filter compensation on the 2 GHz spectrum is quite similar to that shown in Figure 27.

C. Noise

It was desirable to determine the noise level with respect to the mean signal level so that the spectral shape could be accurately analyzed and interpreted. The noise present in the power spectrum can be classified into two types: receiver noise and bit noise. Even though these types of noise are caused by different mechanisms, their effect on the power density spectrum cannot be separated. In this section, two methods are used to determine the noise level in the periodigrams.

Method I. Consider the sampled waveform on a day when the signal was quiet (el. = 43.44°) as shown in Figure 28. A one-bit change on the A/D converter corresponds to 0.13 dB and is discernable in the figure. Note that the A/D converter was toggling one bit above and below the mean signal level (0 dB). This random toggling could have been caused by receiver noise, bit noise, or the atmosphere. However, since a change of only one bit is observed, the receiver noise must be equal to or less than the bit noise.

From the above argument, a waveform which is constant except for a single one-bit toggle should produce a spectrum whose maximum component is a close approximation to the noise level in any given periodigram due to bit toggling. This level was calculated as -81.5 dB below the dc power level.

Method II. Assume that the receiver noise is flat up to 5 Hz and drops to zero above 5 Hz. Then with a system margin of 52 dB and spectral lines spaced 0.00488 Hz apart, the noise level is calculated as

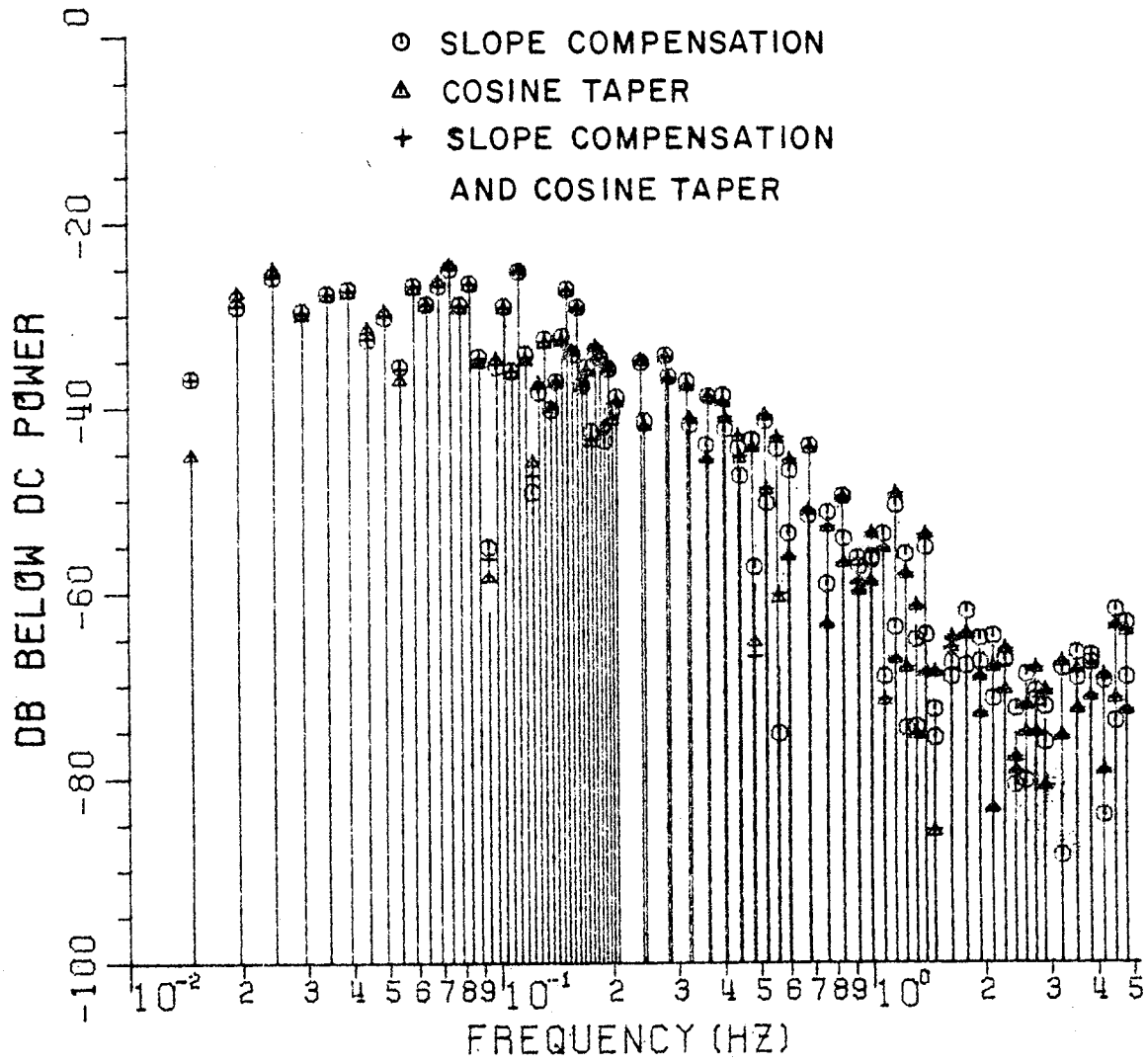

Figure 26. Effect of processing techniques on periodigram.

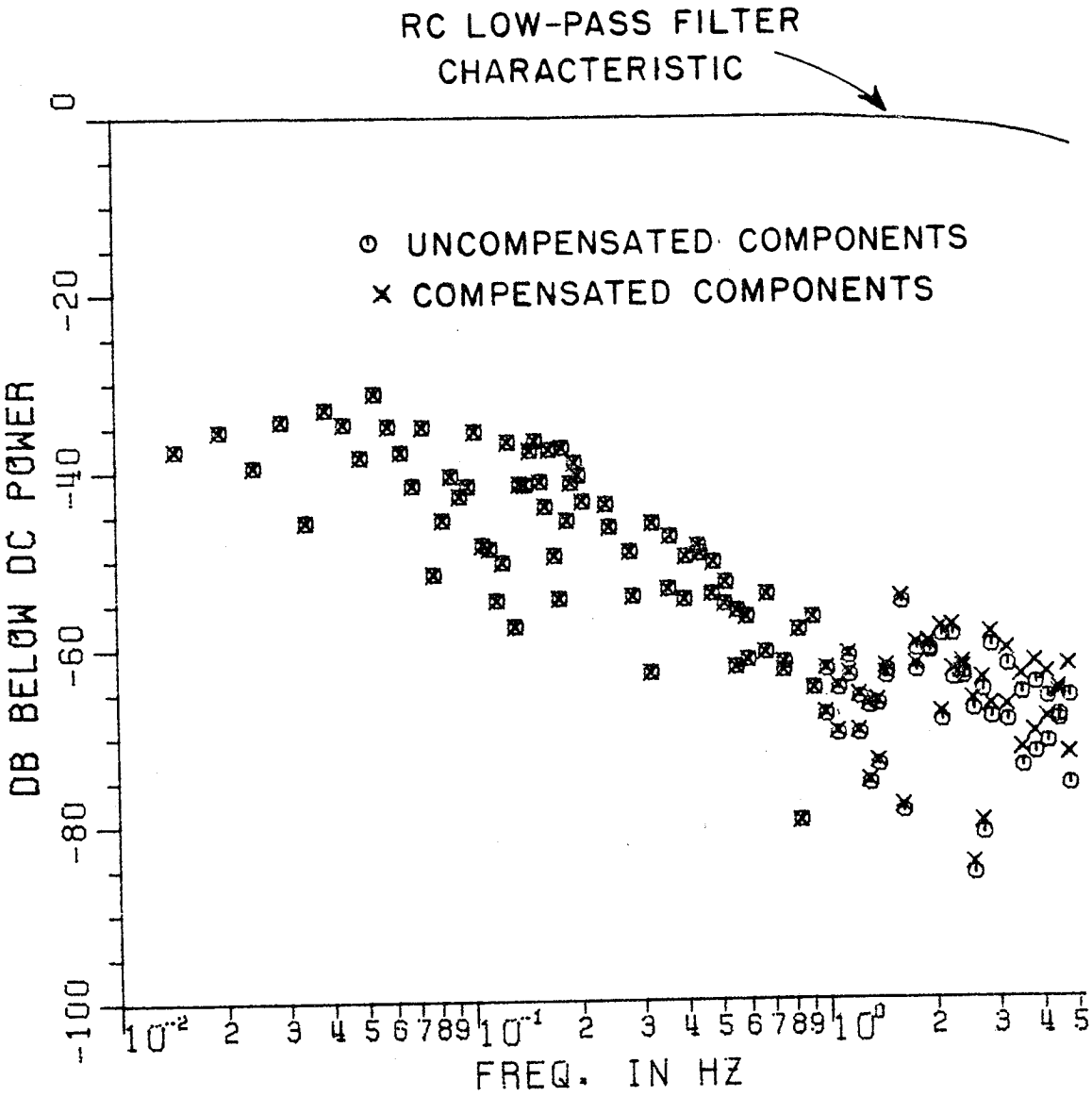

Figure 27. Low-pass filter characteristics and appropriate spectral compensation.

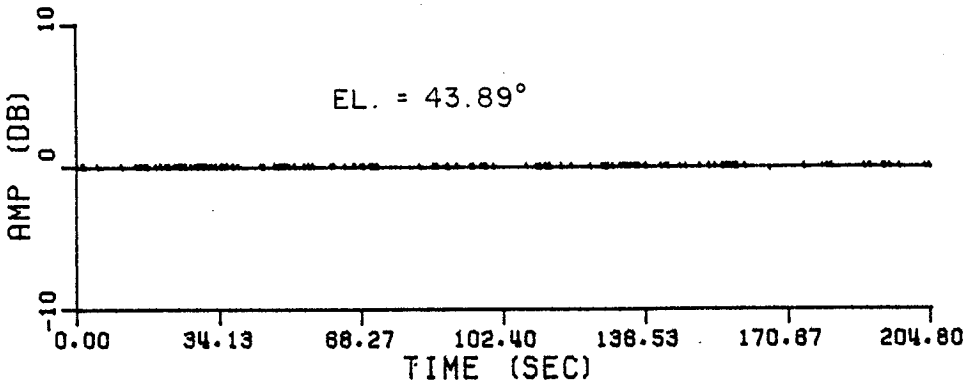

Figure 28. Sampled waveform on a "quiet" day.

$$\text{noise level} = 10 \log_{10}\left(\frac{0.00488}{5}\right) - 52 = -82.0 \text{ dB} \qquad (24)$$

A periodigram of the sampled waveform shown in Figure 28 is shown in Figure 29. A linear regression line drawn through the spectral components intersects the ordinate at -76 dB.

Considering the noise levels given above, a threshold level at which the noise "corrupts" the spectrum was first set at -80 dB. However, after examining the results of slope and break frequency calculations (discussed in the next chapter), this "noise cutoff level" was raised to -70 dB below the dc power level, which corresponds to the peaks of the spectral components in Figure 29.

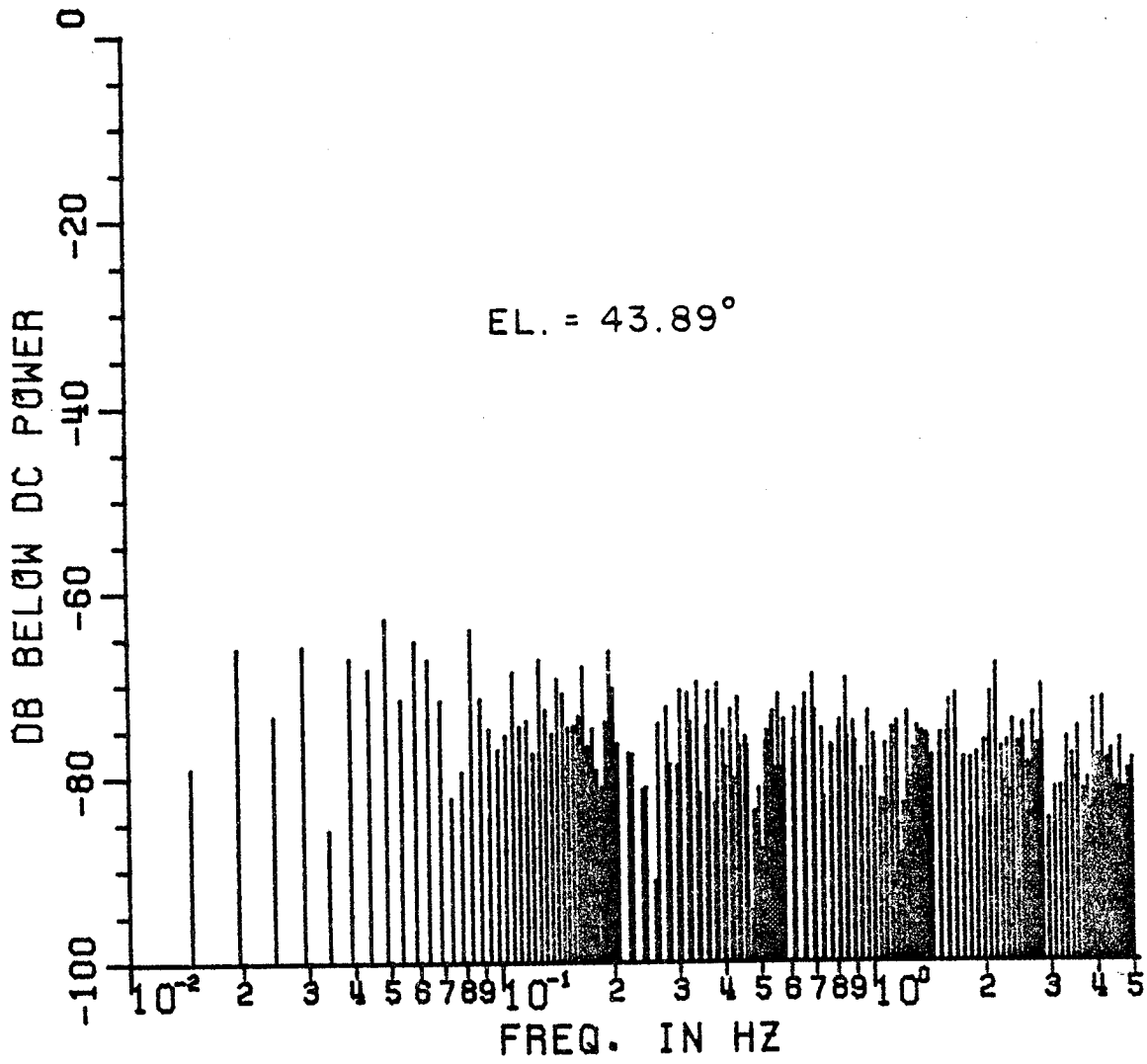

Figure 29. Periodigram of "quiet" sampled waveform.

CHAPTER V

RESULTS

In this chapter the spectral characteristics of the experimental data are investigated. A comparison is made between the experimental results and the theoretical results discussed in Chapter II. The spectra are characterized by either one or two slopes which are obtained by a linear regressive (least squares) fit. Probability density functions are given for slopes and, in the case of two-slope fits, break frequencies. The dependence of the spectral shapes and break frequencies on elevation angle (path length) is also investigated.

A. Approach

The basic approach was to process the time-domain digital waveform using the techniques described in Chapter IV to obtain a reasonably accurate power density spectrum.

The next step was to fit the spectra to a shape similar to that shown in Figure 3. Note that the lower break frequency in Figure 3 is dependent on the rate of change of the real and imaginary parts of the refractive index with respect to temperature, $\partial a/\partial T$ and $\partial b/\partial T$ respectively. The values for these quantities are calculated in Appendix B using oxygen and water vapor as the absorptive gases. These values were used in Equation (16) to compute the lower break frequency, f_{b1}. The results of these calculations for 50% humidity at an elevation angle of 20^{o} are given in Table III. The values of f_{b1} given in Table III are several orders of magnitude lower than those calculated by Ott[14] using oxygen as the only absorptive gas; the reason for this discrepancy is unknown at this time.

Table III
Lower Break Frequency (el. = 20^{o})

Frequency (GHz)	$\partial a/\partial T/\partial b/\partial T$	f_{b1} (Hz)
2.075	5.02×10^{4}	4.71×10^{-10}
30.000	6.89×10^{3}	2.09×10^{-9}

The above calculation indicates that the lower break frequency should not be seen in the periodigrams. Therefore, a maximum of two slopes were fit to the spectra.

Two slopes were fit to the spectra by an iterative procedure based on the minimum of the root-mean-squared (r.m.s.) errors of each regression. The first fit, characterized by a slope, A1, and intercept, P_i, was obtained by setting the break frequency (the frequency at which the two slopes intersect), f_b, equal to the eleventh harmonic*, performing a linear regression on the first eleven harmonics and then performing a second linear regression, characterized by a slope, A2, constrained about the point at which the first regression curve intersected a vertical line drawn through the break frequency, see Figure 30.

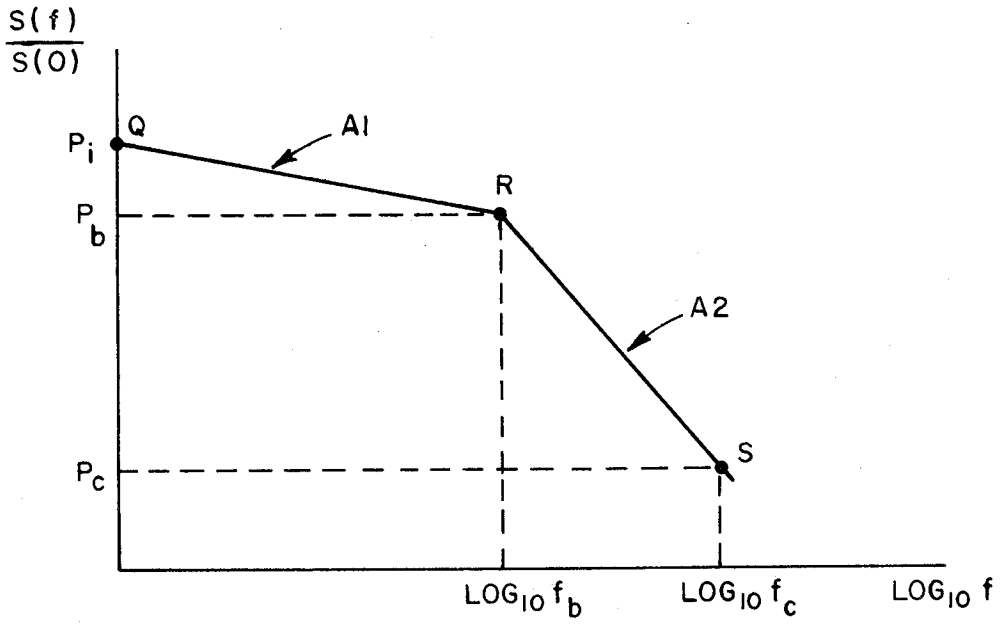

Figure 30. Geometry of two-slope fit.

Each successive fit was obtained by incrementing the harmonic number and fitting two more slopes. After obtaining the slopes for the maximum harmonic number, r.m.s. errors at each break frequency were compared. The slopes obtained with the minimum r.m.s. error were considered the best fit, and the harmonic frequency at which the best fit was found was taken as the break frequency.

*The eleventh harmonic (0.0537 Hz) was chosen as the first usable break frequency to ensure that at least ten points were used for the first regression.

By visually examining several spectra, the maximum harmonic number for the break frequency search was set at 250, which corresponds to f_{max}=1.22 Hz. The break frequency harmonic was not allowed to come closer than ten harmonics within the harmonic corresponding to the noise cutoff frequency. The break frequency search algorithm along with the noise cutoff algorithm is given in Appendix A.

After obtaining two slopes and a break frequency, a noise cutoff level adjustment was made to prevent the slopes from being contaminated by the noise in the spectrum discussed in Chapter IV. From the results presented in the last section of Chapter IV, the level at which the noise corrupted the spectrum was -70 dB. Therefore, the levels at each point on the regression lines for the spectral slopes were compared with the noise cutoff level. The frequency at which the calculated slope lines intersected the noise cutoff level line (point S in Figure 30) was termed the noise cutoff frequency, f_c. Once f_c was determined, the entire break frequency search procedure was repeated; however, only the harmonic numbers below that corresponding to f_c were used in the regressions.

Figures 31 through 35 show two-slope fits as calculated from typical samples. In Figures 32a, 33a, and 34a it is obvious that the two slopes do not accurately represent the spectrum. The problem is most probably in the error minimization criterion and in allowing the break frequency to come too close to the noise cutoff frequency.

Because of the problems with the break frequency search routine, the results were visually classified into four types: (1) A1 > A2, (2) A1 < A2, (3) A1 $\approx$ A2, and (4) other unacceptable cases due to difficulties in the computer algorithm. The type (3) cases were recalculated using a single linear regression curve fit (the single slope regression algorithm is given in Appendix A). Only type (1) cases were used for break frequency statistics. Slope statistics were found from the second slope of type (1) cases, and the first slope of the type (2) and (3) cases. The second slopes of the type (2) cases were assumed to be caused by noise in the spectrum and, thus, were not used. All type (4) cases were considered unusable. The statistics of the data sets are given in Table IV.

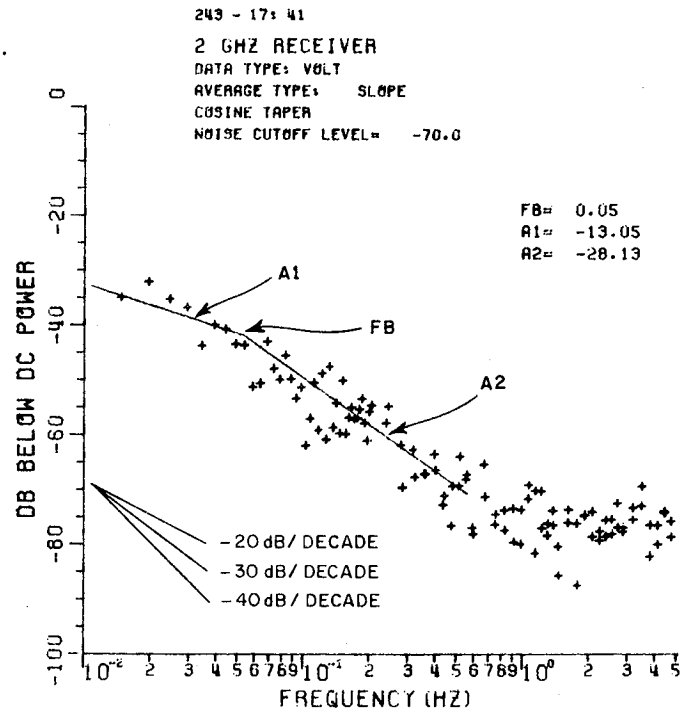

(a)

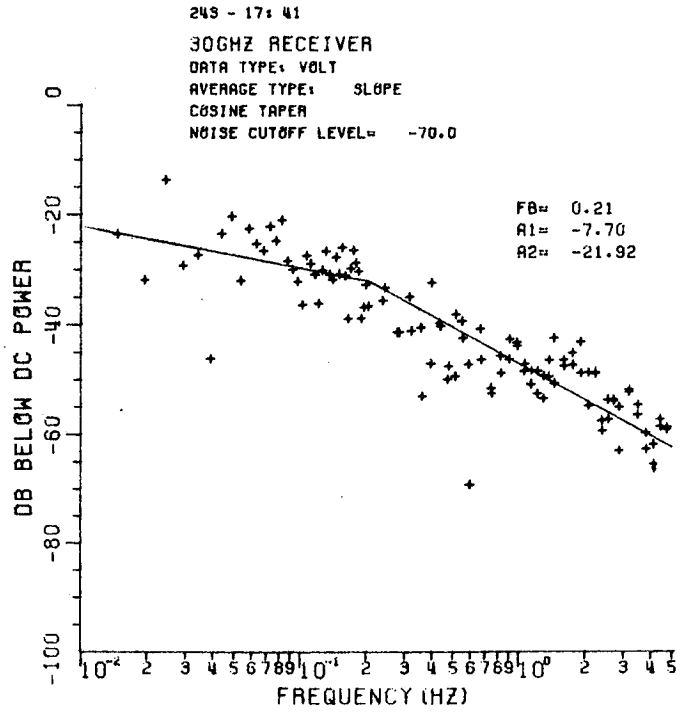

(b)

Figure 31. Two-slope fit at el. = 0.38^{o}.

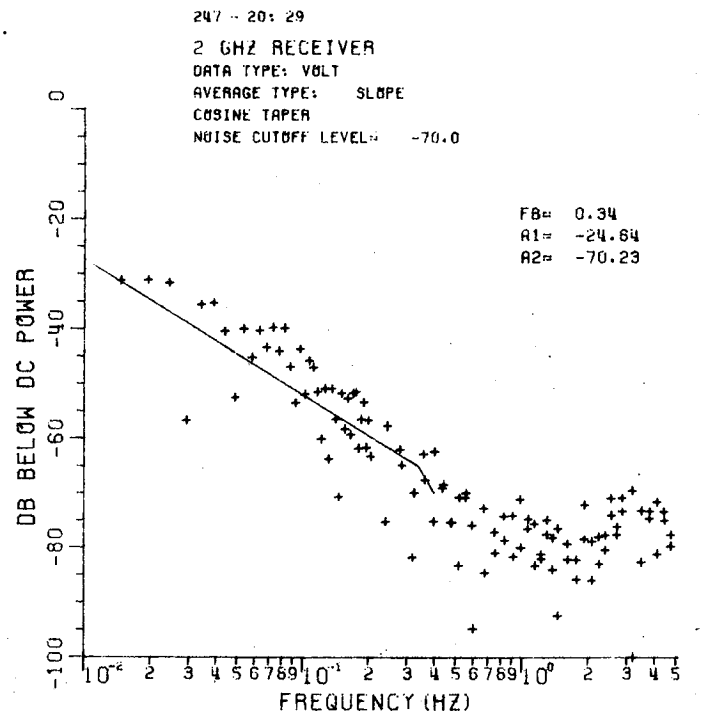

(a)

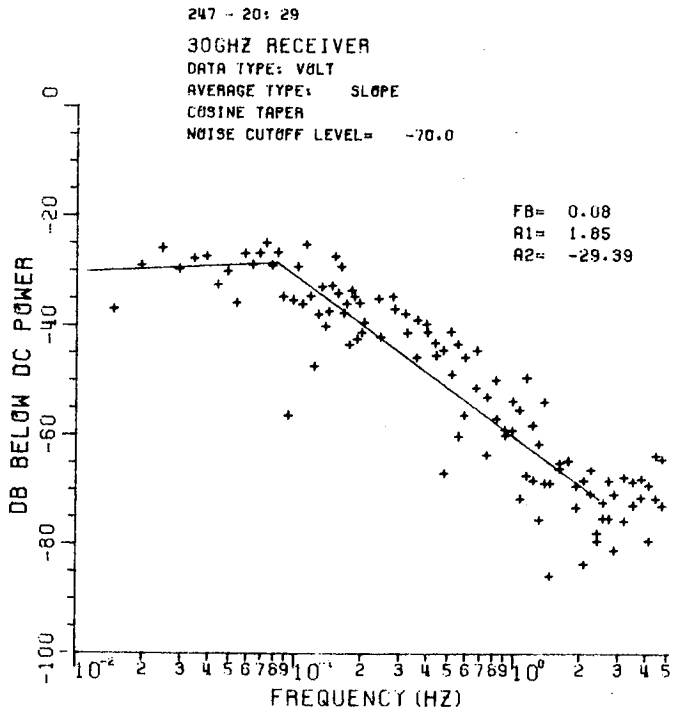

(b)

Figure 32. Two-slope fit at el. = 4.95^{o}.

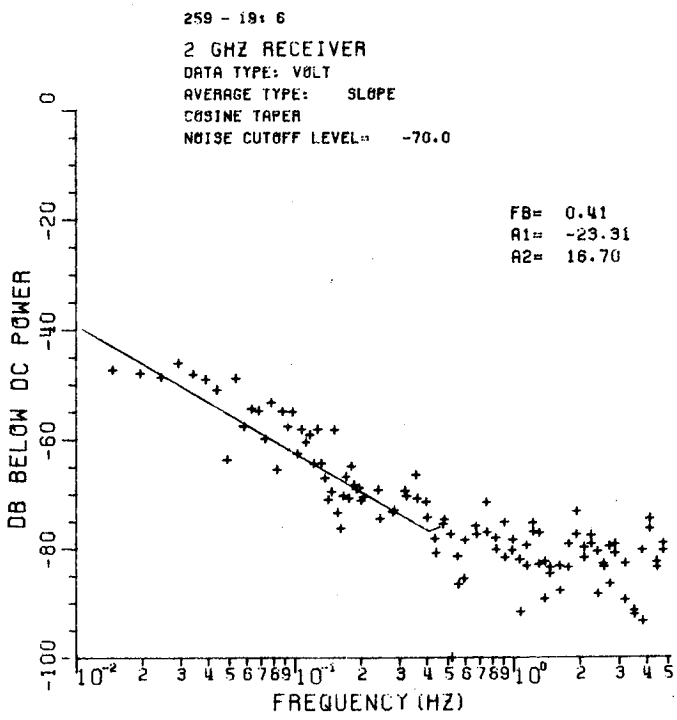

(a)

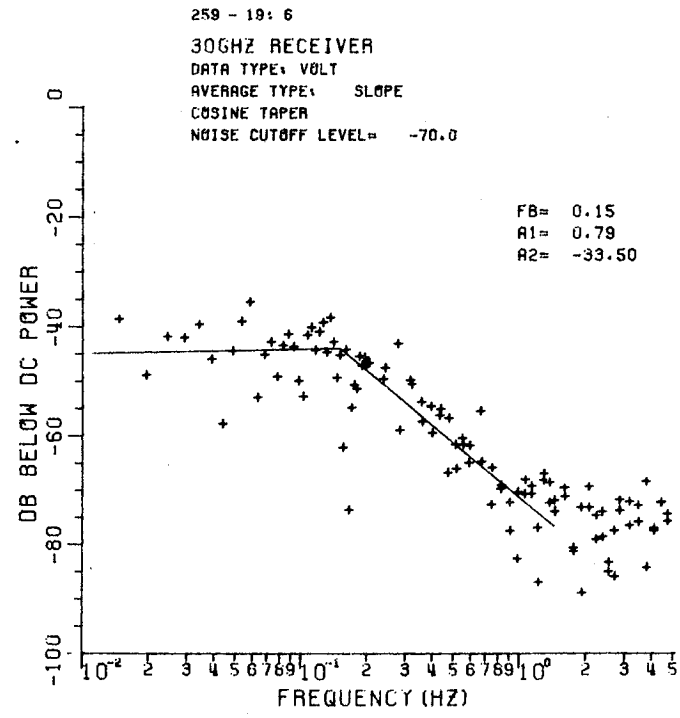

(b)

Figure 33. Two-slope fit at el. = 18.11°.

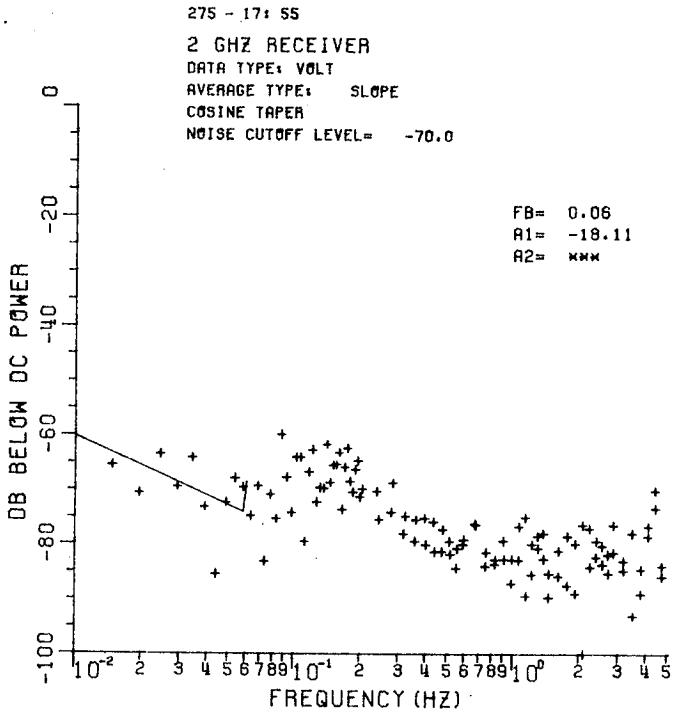

(a)

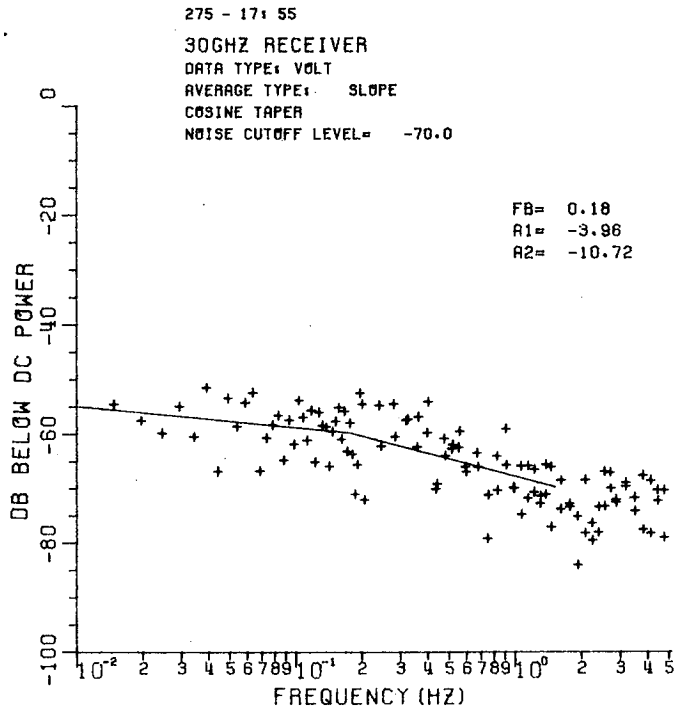

(b)

Figure 34. Two-slope fit at el. = 33.65^{o}.

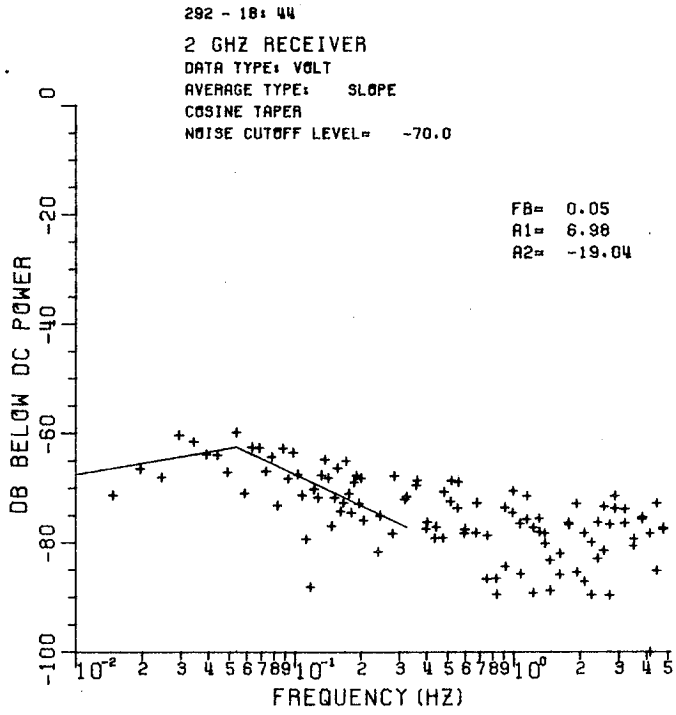

(a)

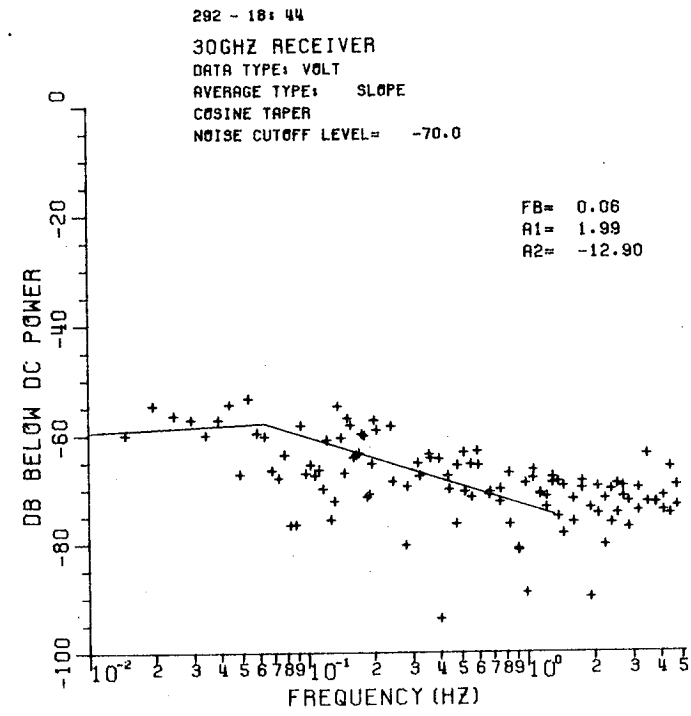

(b)

Figure 35. Two-slope fit at el. = 43.44^{o}.

Table IV
Results of Data Classification

Type	No. of Cases at 2 GHz	No. of cases at 30 GHz
1	142	238
2	119	53
3	112	117
4	98	62
Total	471	470

B. Probability Density Functions

In Chapter II it was shown that the spectral slopes should roll off according to $f^{-8/3}$, which corresponds to -26.7 dB/decade on the periodigrams. In this section, the distribution of the slopes and break frequencies are described by probability density functions. Figures 36 and 37 show the slope probability density functions. The mean of the 2 GHz data is -23.5 dB/decade and -21.8 dB/decade for the 30 GHz data. The distributions about these means are quite different. The 2 GHz data has a very high peak at -25 dB/decade and has a wide range. The 30 GHz data does not contain a single high peak as seen in the 2 GHz data; in fact, the 30 GHz data exhibits a double peak behavior. This type of behavior might be the result of bit noise contamination, i.e., the density to the left probably corresponds to turbulence-induced spectra while the density to the right might be the result of spectra contaminated by bit noise.

There are several possible explanations for the average value of slope to be less steep than the theoretical value. Random bit toggling would cause the spectral slope to approach -20 dB/decade or flatter (see Appendix C). Aliasing would tend to enhance the higher frequency components which would also make the slopes less steep. Causes of the variations in slope might include spatial and temporal inhomogeneous turbulence, changes in average wind direction, and nonstationarity of the process.

The break frequency probability density functions are shown in Figures 38 and 39. Note that the bulk of the frequencies is at the lowest value that can be obtained from the break frequency search algorithm. This high density toward the lower values suggests that there might be a significant number of break frequencies just below the minimum value. Also, since the wind speed data have a fairly symmetric distribution, the break frequencies

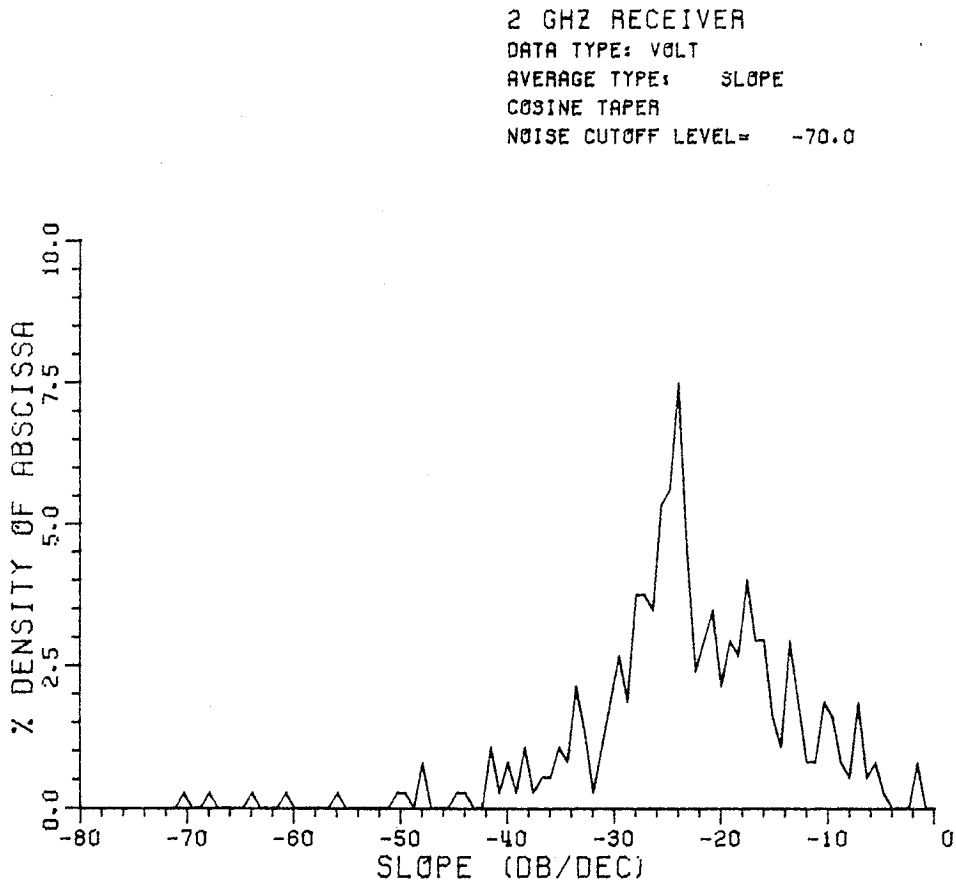

Figure 36. Probability density function of spectral slopes for 2 GHz receiver.

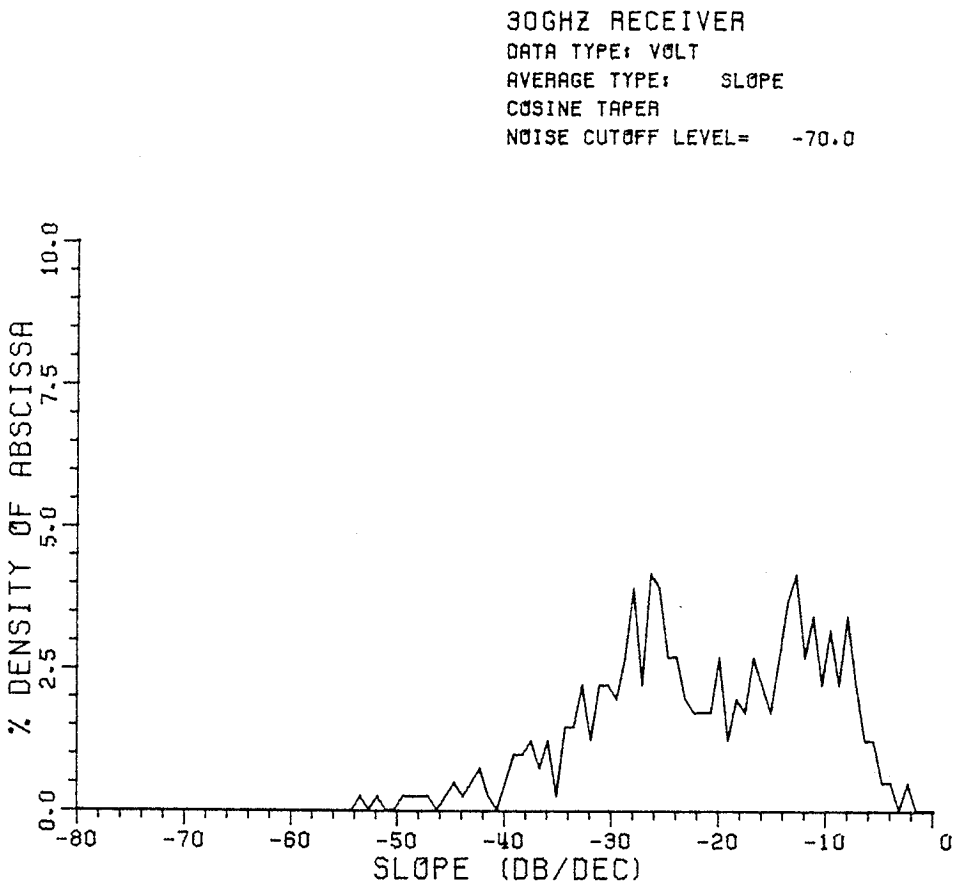

Figure 37. Probability density function of spectral slopes for 30 GHz receiver.

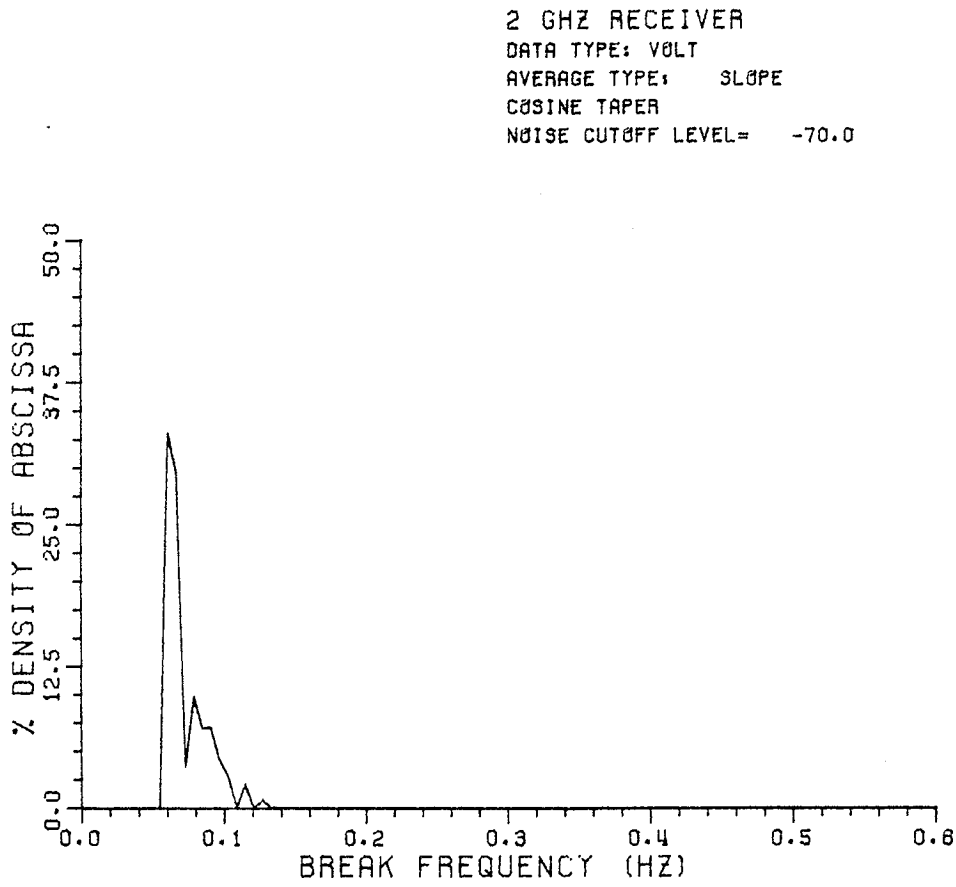

Figure 38. Probability density function of spectral break frequency for 2 GHz receiver.

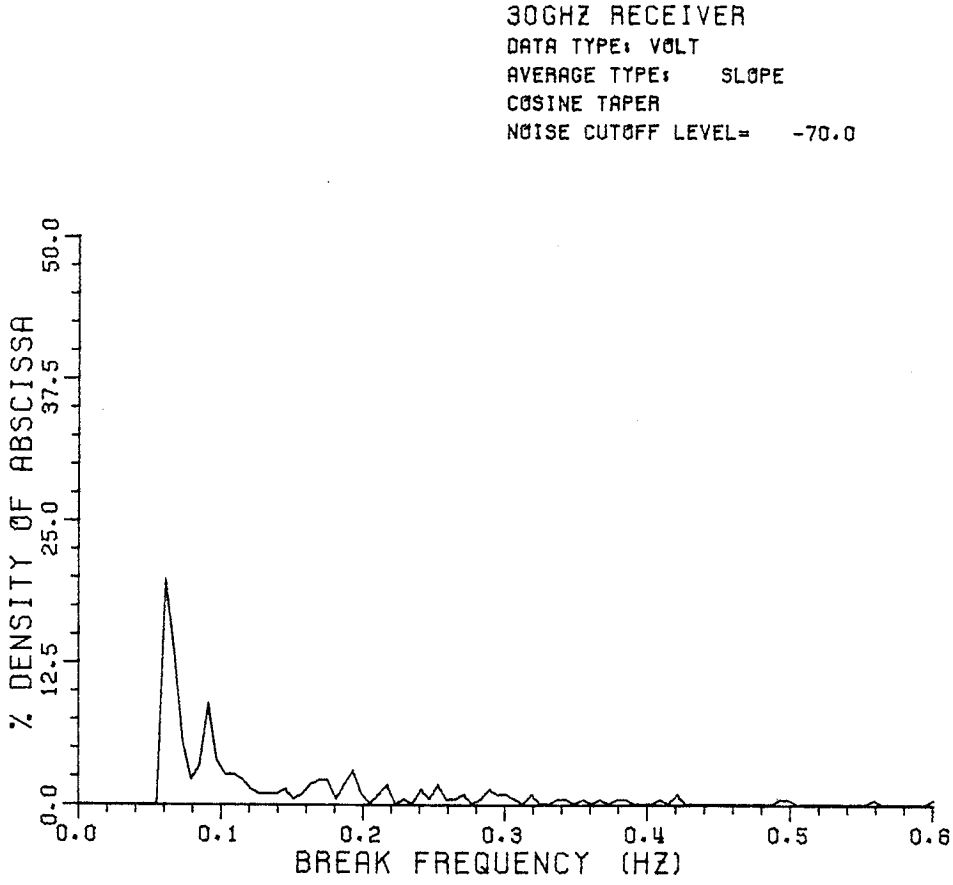

Figure 39. Probability density function of spectral break frequency for 30 GHz receiver.

should also have a fairly symmetric distribution. Thus, some of the break frequencies might represent second order break frequencies. For example, if the actual break frequency was below the minimum (0.05 Hz), then the break frequency search would attempt to find a break frequency higher than 0.05 Hz.

The range of values of break frequencies is quite reasonable when compared with break frequencies corresponding to appropriate wind speed data. For example, a break frequency of 0.1 Hz for the 30 GHz data corresponds to a perpendicular wind speed of 1.54 m/sec at an elevation angle of 20^{0}. For the 2 GHz data, a break frequency of 0.1 Hz corresponds to a perpendicular wind speed of 2.38 m/sec.

Since wind speed was recorded on a strip chart and wind speed and direction was also available from the weather bureau (about 4 miles east of the receiving terminal) a comparison between measured wind speeds perpendicular to the signal path and wind speeds calculated from the break frequency data was made. However, the correlation was quite low, particularly at the low elevation angles; the wind speeds calculated from break frequencies were mostly greater than those measured directly. A poor correlation was not surprising since the measured wind speeds were point measurements on the ground and the calculated wind speeds represent an average value along the signal path. For this reason, inhomogeneities in the atmosphere could cause poor correlation between measured and calculated wind speeds, especially at the low elevation angles.

C. Dependence of Spectral Characteristics on Elevation Angle

According to the discussion in Chapter II, the spectral slopes should obey the $f^{-8/3}$ (-26.7 dB/decade) law. No dependence on elevation angle is found in the weak fluctuation theory. However, as mentioned earlier, the 30 GHz data at low elevation angles (below 4^{0}) does not satisfy the weak fluctuation criterion according to Ishimaru. The strong fluctuation theory predicts a spectral slope proportional to f^{0} or 0 dB/decade (see Appendix D). It is not clear at this point how the strong fluctuation theory interfaces with the weak fluctuation theory.

Figures 40 and 41 show the dependence of spectral slope on elevation angle. The crosses represent maximum and minimum values and the circles are the average slopes, in dB/decade, at each elevation angle. The dashed line indicates the theoretical -26.7 dB/decade slope, and the solid line represents the average value of all measured slopes. The effective path length scale is based on a spherical earth model with a 4/3 radius and a homogeneous atmosphere of 6 Km. The effective path lengths ranged from 8.6 Km to 318 Km.

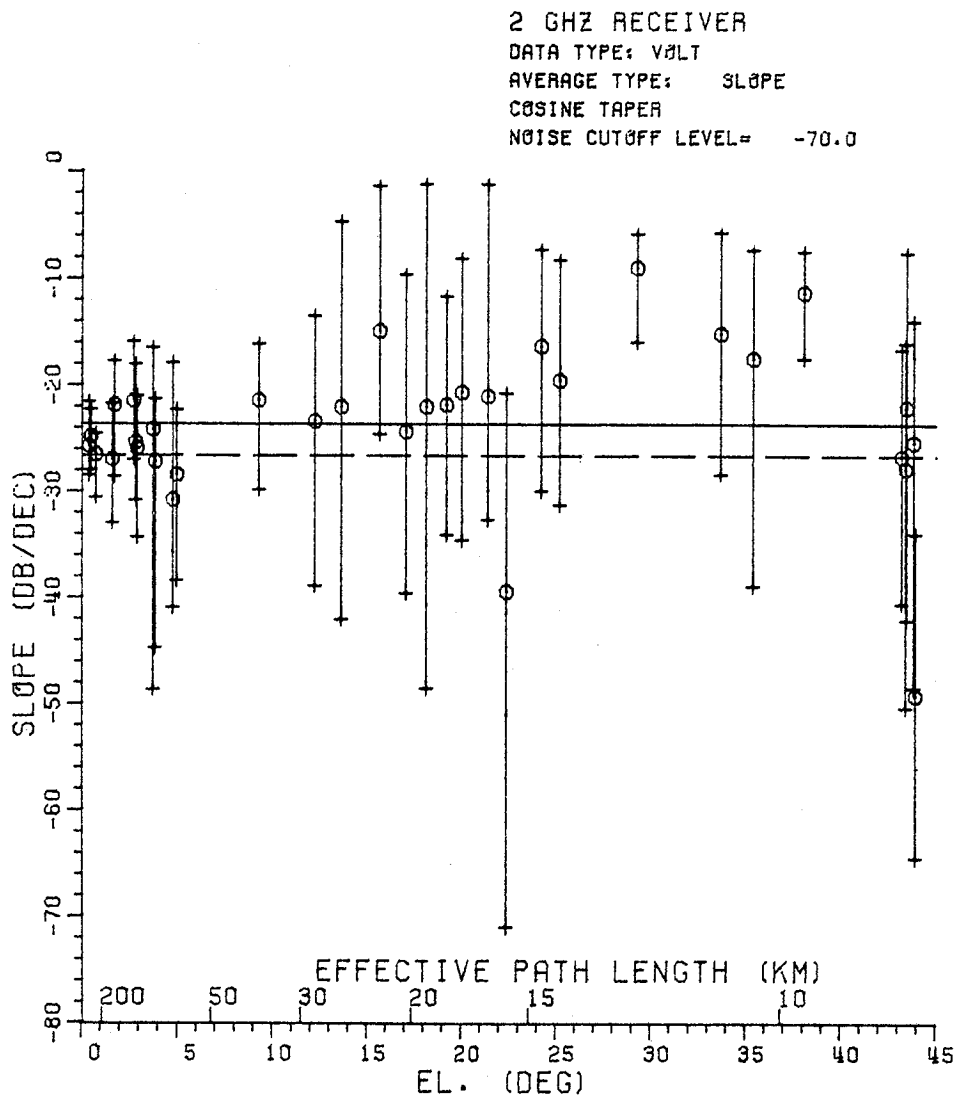

Figure 40. Dependence of spectral slope on elevation angle for 2 GHz receiver.

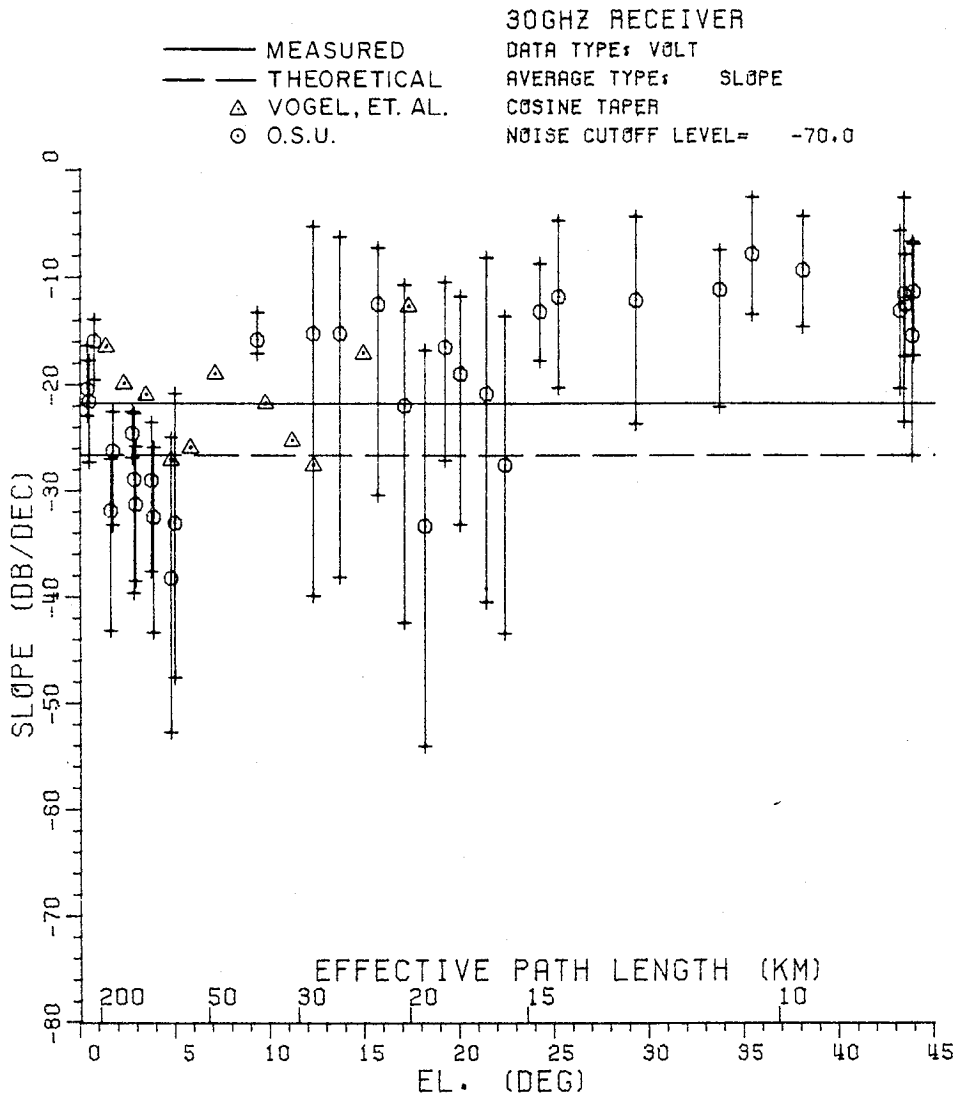

Figure 41. Dependence of spectral slope on elevation angle for 30 GHz receiver.

The 2 GHz data has a quite large maximum-to-minimum spread, although the average is quite close (3.2 dB/decade above) to the theoretical value. The average points at the low elevation angles and at the high elevation angles are in good agreement with theory. Most average points between the elevation angle extremes are several dB/decade higher than the theoretical value.

The 30 GHz slopes have a much narrower maximum-to-minimum spread. Data taken by Vogel, Straiton and Fannin[18] is also shown in Figure 41. Both data sets seem to be in fairly good agreement, with the data taken by Vogel, et al. tending to have less steep slopes at the lower elevation angles. It is unknown whether the fact that the data obtained by Vogel, et al. was measured over water might have caused less steep slopes at low elevation angles.

Note that there seems to be a trend toward steeper slopes from el. = 0.38^{o} to el. = 5^{o}. This trend is also apparent in the data taken by Vogel, et al. This trend might have something to do with strong fluctuations; however, the slopes do not approach 0 dB/decade as predicted by the strong fluctuation theory. Aperture averaging might also be an influence of this trend since aperture averaging would reduce the small-scale fluctuations which would in turn cause steeper slopes.

Immediately following 5^{o}, the slopes show a sudden change toward less roll off. The data taken by Vogel, et al. also shows this sudden change, but it is not as pronounced as the O.S.U. data. This sudden change in values seem to suggest a transition region between two mechanisms; for example, between strong and weak fluctuations or between angle-of-arrival fluctuations and amplitude fluctuations.

The slopes above 5^{o} are mostly flatter than the theoretical value. The reason for this is again probably due to bit noise.

The 2 GHz break frequencies as a function of elevation angle are shown in Figure 42. The spread is seldom more than 0.05 Hz, and, as pointed out in the p.d.f.'s, most of the break frequencies are close to the lowest possible frequency which could be obtained from the break frequency search algorithm.

The 30 GHz break frequencies as a function of elevation angle are shown in Figure 43. The spread is much more than the 2 GHz data, sometimes as much as a factor of 20 greater than the 2 GHz data. The 30 GHz break frequencies are not as heavily concentrated about the lowest value as would be expected if the break frequencies are indeed related to the perpendicular wind speeds as given in Equation (13) (Chapter II).

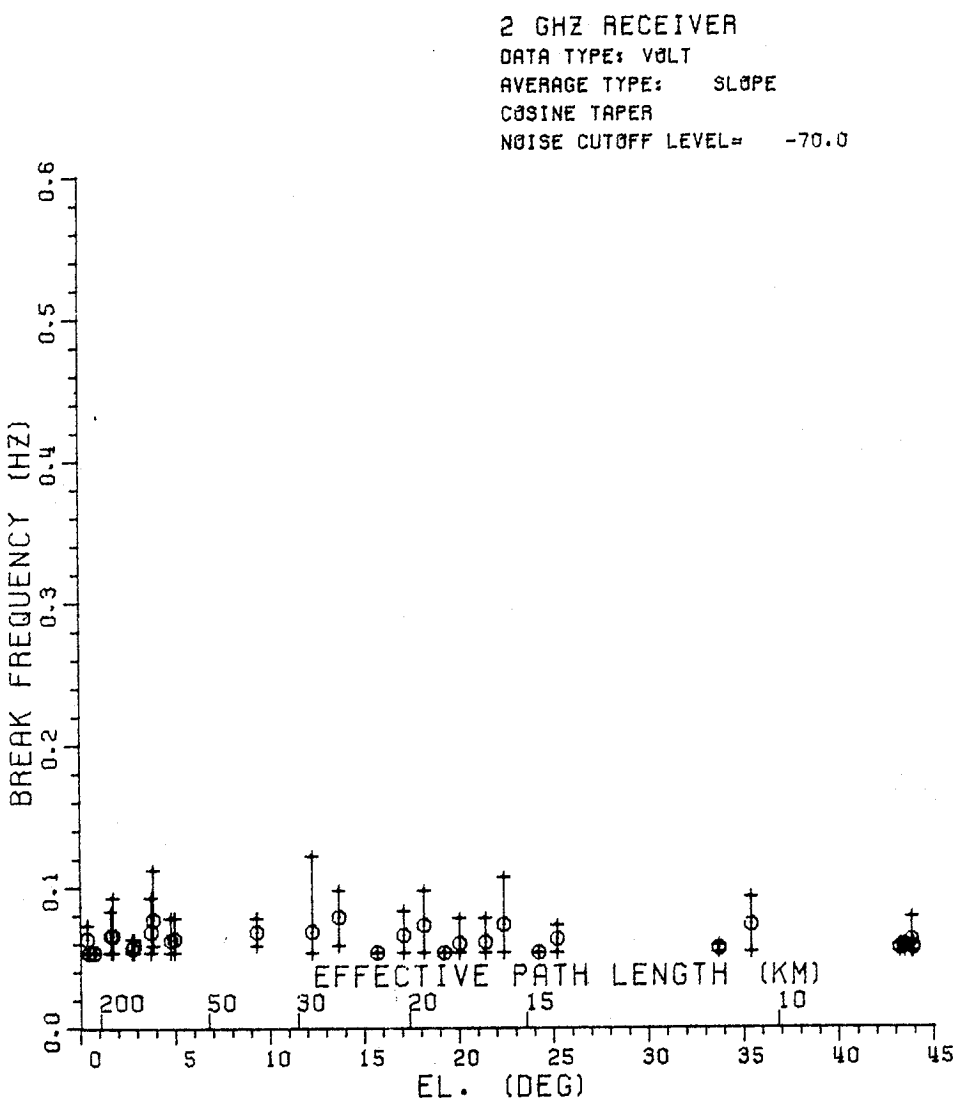

Figure 42. Break frequency as a function of elevation angle for 2 GHz receiver.

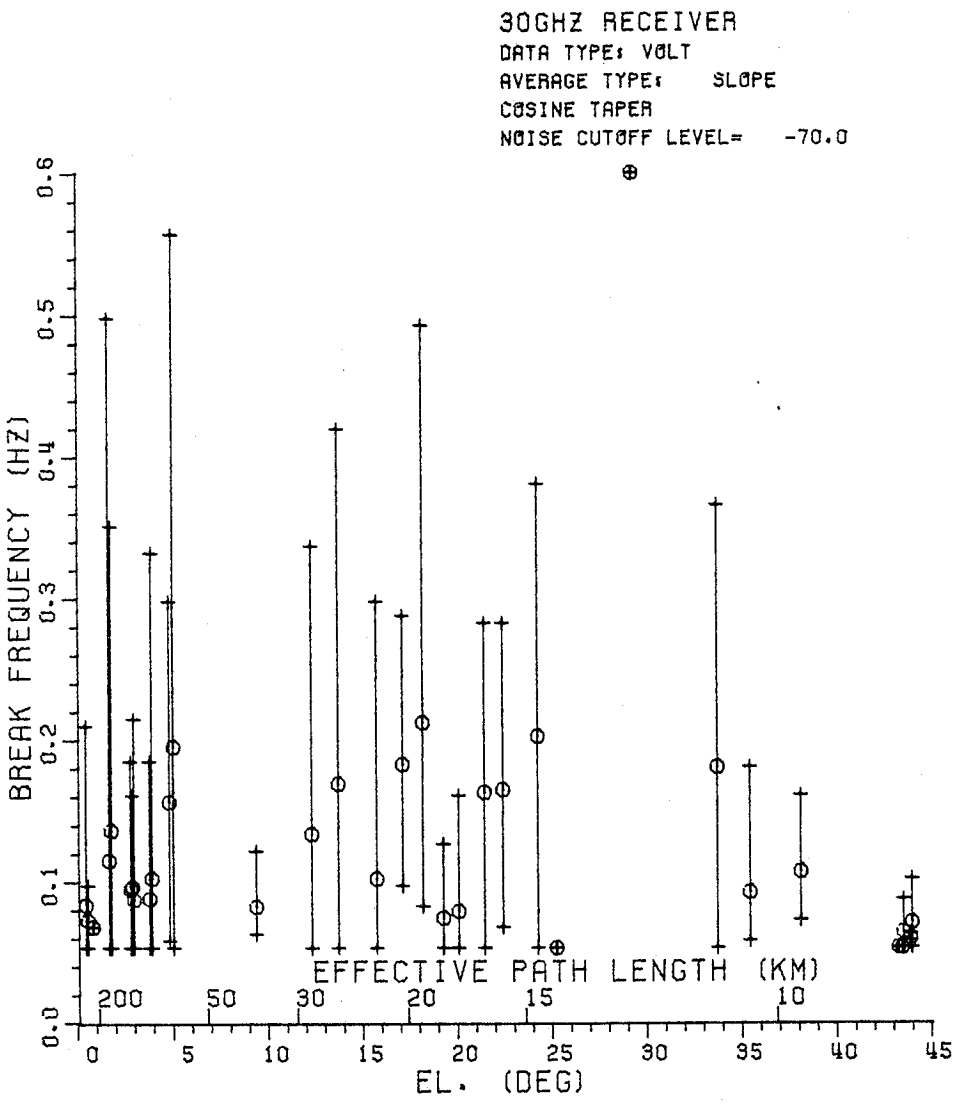

Figure 43. Break frequency as a function of elevation angle for 30 GHz receiver.

D. Comparison of Spectral Characteristics between 2 and 30 GHz Data

To gain a better insight as to the nature of the data, the spectral characteristics at 2 GHz and those at 30 GHz were compared visually from scatter plots. Figure 44 shows a scatter plot of the 30 GHz slope versus the 2 GHz slope. Theoretically, the spectral slopes should be -26.7 dB/decade at both frequencies. This scatter plot shows that the slopes are indeed heavily concentrated around the theoretical value.

Figure 45 shows a scatter plot of the 30 GHz break frequency versus the 2 GHz break frequency. Theoretically, the ratio of the 30 GHz break frequency to the 2 GHz break frequency is 3.87, as indicated by the dashed line. The solid line represents a linear regression through the scatter points. The agreement with theory is quite close even though the lowest attainable break frequency is most likely too high.

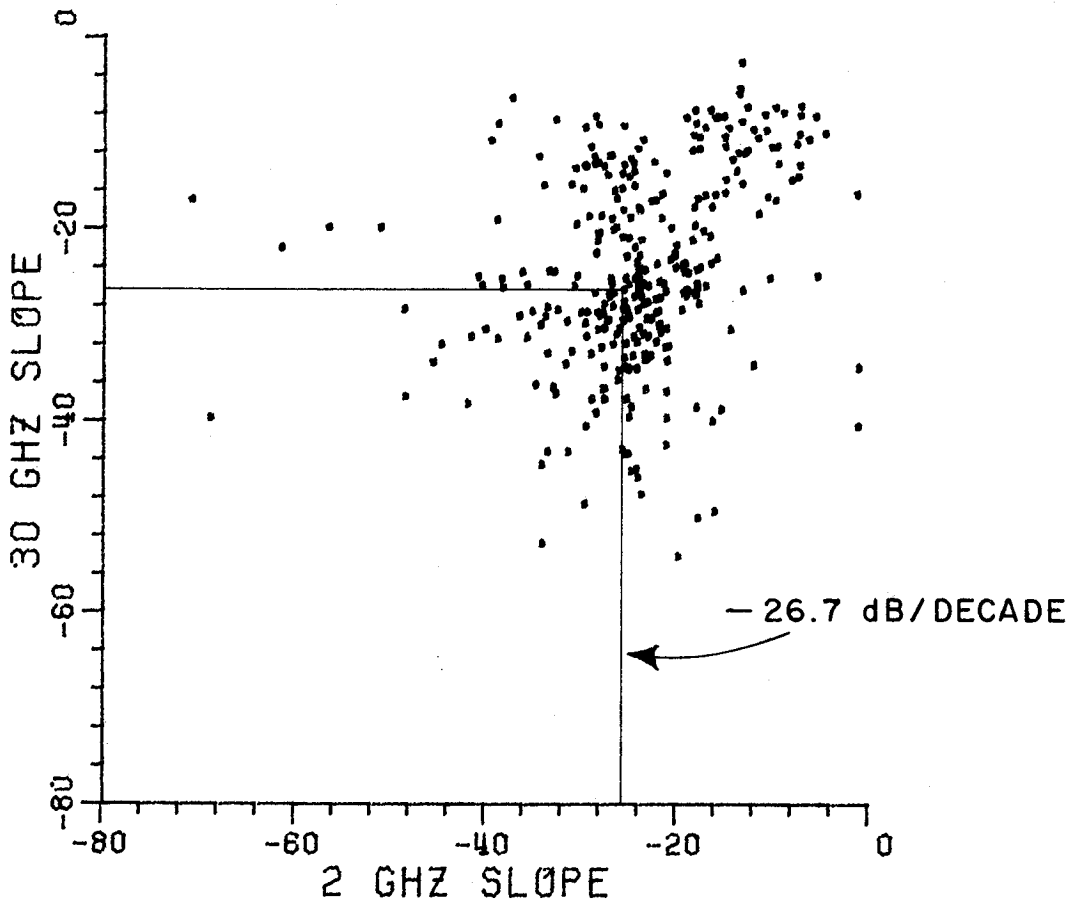

Figure 44. Scatter diagram of 30 GHz spectral slope versus 2 GHz spectral slope.

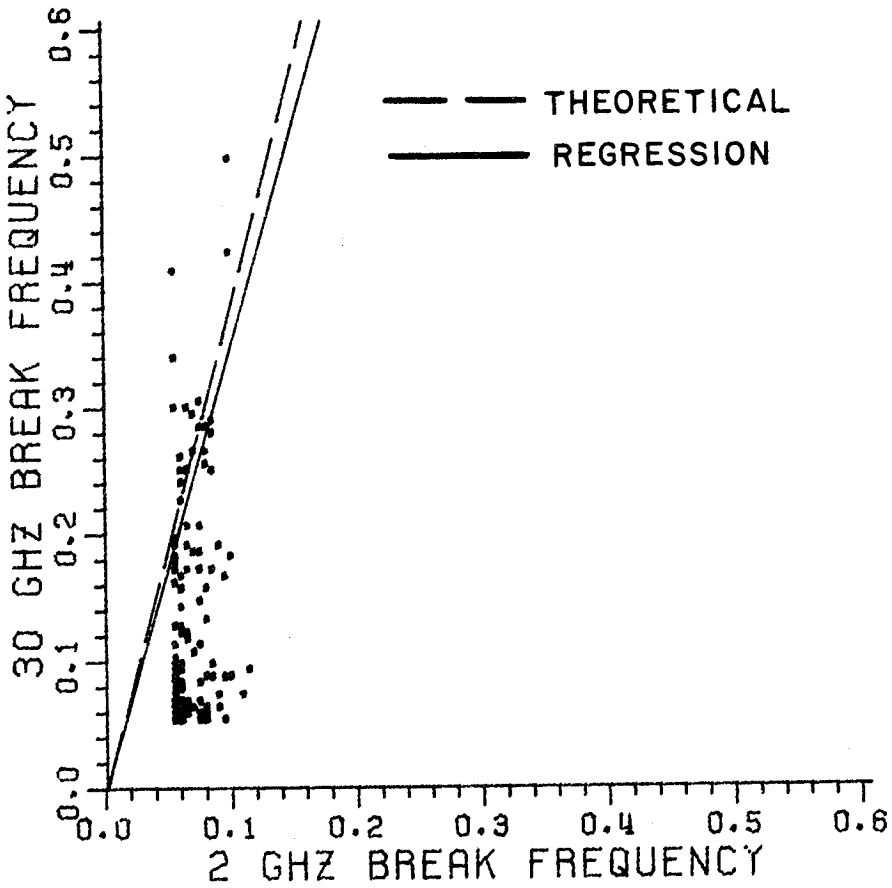

Figure 45. Scatter diagram of 30 GHz break frequency versus 2 GHz break frequency.

CHAPTER VI

SUMMARY

The results presented herein characterize spectra of 2 and 30 GHz signals received from the ATS-6 at elevation angles ranging from 0.38° to 44°.

The spectra of the received signals are characterized by a two-slope linear regressive fit and a break frequency corresponding to the intersection of the two slope lines. Cases in which the two slopes were approximately equal were recalculated for a single slope fit. The results are presented statistically in the form of probability density functions. The dependence of the spectral characteristics on elevation angle is given. Scatter diagrams are used to compare the 2 and 30 GHz results.

Average spectral characteristics are in general agreement with predictions based on turbulence theory; however, variations of the slopes can be quite large. In fact, temporal variations of spectral slopes are very similar to variations of the refractive index structure constant[17]. Possible causes for variations in slope include spatial and temporal inhomogeneous turbulence, changes in average wind direction, and nonstationarity of the process.

A trend toward steeper slopes appears to be evident at low elevation angles (below 5°) in the 30 GHz data. The cause and certainty of this behavior is unknown at this point and should be carefully examined in future experiments.

Because the time-domain waveforms are mostly low-order bit toggles at elevation angles greater than 25°, the spectral slopes and break frequencies above 25° are probably biased representations of the spectral characteristics.

APPENDIX A

COMPUTER ALGORITHMS

The following routines are computer algorithms which implement the techniques discussed in this thesis.

	Technique	Subroutines used	Lines
1.	Slope compensation	MEAN	1-40
2.	Cosine taper	COSTAP	44-60
3.	Power density spectrum	FFT	64-106
4.	Break frequency search	CORRUPT,BREAK	111-182
5.	Single slope regression	ONESLP	186-213
6.	Regressions	LINREG,CLR	217,298

```
      SUBROUTINE MEAN(Y,KAV,AV1)
C
C     SLOPE COMPENSATION
C
C     KAV=0:POINT AVERAGE
C     KAV=1:SLOPE COMPENSATION
C
C     Y   -- TIME-DOMAIN SAMPLED WAVEFORM
C     KAV -- AVERAGE TYPE
C     AV1 -- MEAN OF SAMPLED WAVEFORM
C
      DIMENSION Y(2048)
      DATA NEND/100/
      AV1=0.
      IF(KAV.EQ.0) GO TO 30
C     CORRECT FOR SHIFTS OF MEAN LEVEL BY SAMPLING NEND POINTS
C     FROM TIME-DOMAIN WAVEFORM
      AV2=0.
      MPOINT=2048-NEND
      DO 10 I=1,NEND
      AV1=AV1+Y(I)
      K=MPOINT+I
   10 AV2=AV2+Y(K)
      AV1=AV1/NEND
      AV2=AV2/NEND
      AVD1F=(AV2-AV1)/(2048-NEND)
      AVCON=AV1-AVD1F*(NEND/2.)
      DO 20 I=1,2048
   20 Y(I)=Y(I)-AVCON-(AVD1F*I)
      AV1=(AV1+AV2)/2.
      RETURN
C     CALCULATE MEAN OF SAMPLED WAVEFORM AND SUBTRACT
C     FROM Y
   30 DO 40 I=1,2048
   40 AV1=AV1+Y(I)
      AV1=AV1/2048
      DO 50 I=1,2048
   50 Y(I)=Y(I)-AV1
      RETURN
      END
C
C
C
      SUBROUTINE COSTAP(Y,M,N)
C
C     COSINE TAPER
C     TIME-DOMAIN SAMPLED WAVEFORM
C     M=NUMBER OF SAMPLES TO BE TAPERED ON EACH END OF RECORD
C     N=NUMBER OF SAMPLES
C
      DIMENSION Y(1)
      A=PI(1.)
      DO 10 I=1,M
      J=N+1-I
      B=A*(M-I)/M
```

```
      C=.5*(1.+COS(B))
      Y(I)=Y(I)*C
10    Y(J)=Y(J)*C
      RETURN
      END
C
C
C
      SUBROUTINE FFT(X,Y,S)
C
C     PRODUCE PERIODIGRAM FROM SAMPLED WAVEFORM
C     USING FFT (FORT)
C
C     X -- ARRAY OF HARMONIC FREQUENCIES
C          (MULTIPLES OF TLF)
C     Y -- TIME-DOMAIN SAMPLED WAVEFORM
C     S -- ARRAY OF SPECTRAL COMPONENTS
C
      COMPLEX B
      COMMON/ARAYS3/B(2048),SS(512)
      DIMENSION X(1024),Y(2048),S(1024)
      COMMON/SET1/NEREQ,NRATE,TLF
      COMMON/SET3/NDTYP,MATCH,NTAP,KAV,CUTOF,AV1,NFD
      DATA NPNTS/2048/,NHF/1024/,M/11/
      TLF=FLOAT(NRATE)/FLOAT(NPNTS)
C     SET UP SINE TABLE
      CALL FORT(B,M,SS,0,IFERR)
      DO 5 I=1,NPNTS
      B(I)=CMPLX(Y(I),0.)
5     CONTINUE
C     FAST FOURIER TRANSFORM SAMPLED WAVEFORM
      CALL FORT(B,M,SS,-2,IFERR)
      IF(IFERR.NE.0)NERR=YEP(13HERROR IN FORT,13,0)
C     CALCULATE DC COMPONENT
      DA=REAL(B(1))**2
      DCP=AV1*AV1+DA
C     CALCULATE POWER SPECTRAL COMPONENTS
C     IN DB BELOW MEAN LEVEL
      DO 10 I=2,NHF
      J=NPNTS+2-I
      L=I-1
      SW=2.*REAL(B(I)*B(J))
      S(L)=10.*ALOG10(SW/DCP)
      XC=TLF*L
      X(L)=ALOG10(XC)
10    CONTINUE
C     CORRECT SPECTRAL COMPONENTS FOR
C     LOW-PASS FILTER ROLL-OFF
      CALL BWCOR(X,S)
      RETURN
      END
C
C
C
C
```

```
      SUBROUTINE CORUPT(CLIF,CUTOF)
C
C     NOISE CUTOFF ADJUSTMENT:
C     FIND NOISE CUTOFF FREQUENCY AND SEARCH
C     FOR BREAK FREQUENCY ONLY UP TO THAT FREQUENCY
C
C      CLIF -- NOISE CUTOFF FREQUENCY (HZ)
C     CUTOF -- NOISE CUTOFF LEVEL (DB)
      COMMON/SET4/FB,A1,B1,A2,ER
      COMMON/ARAYS1/X(1024),Y(2048),S(1024)
      COMMON/ARAYS2/XP(1024),YP(2048),YOUT(1024)
      DATA NHFM1/1023/
      TLF=10./2048.
      DO 10 I=1,NHFM1
   10 IF(YOUT(I).LT.CUTOF)GO TO 20
      CLIF=5.
      RETURN
   20 CLIF=I*TLF
      CALL BREAK(X,S,FB,A1,B1,A2,ER,I)
      RETURN
      END
C
C
C
      SUBROUTINE BREAK(X,Y,FB,A1,B1,A2,ER,NEND)
C
C     BREAK FREQUENCY SEARCH AND TWO-SLOPE FIT
C
C       X -- ARRAY OF HARMONIC FREQUENCIES
C       Y -- ARRAY OF SPECTRAL COMPONENTS
C      FB -- BREAK FREQUENCY
C      A1 -- FIRST SLOPE (DB/DEC)
C      B1 -- POWER LEVEL INTERCEPT (DB)
C      A2 -- SECOND SLOPE (DB/DEC)
C      ER -- TOTAL RMS ERROR
C     NEND-- ENDING HARMONIC FOR SEARCH
C
      DIMENSION X(1),Y(1)
      COMMON/SET1/NFREQ,NRATE,TLF
      COMMON/ARAYS2/E(1024),YP(2048),YOUT(1024)
      DATA NMIN/10/,NMAX/250/
      TLF=10./2048.
      NFB=NMIN
      IMIN=1
      I=0
   10 I=I+1
      NFB=NFB+1
      NDIF=NEND-NFB
      IF(NDIF.LT.10)GO TO 15
C     CALCULATE FIRST SLOPE AND POWER LEVEL INTERCEPT
      CALL LINREG(X,Y,1,NFB,A1,B1,ERR1,YOUT)
C     CALCULATE SECOND SLOPE
      CALL CLR(X,Y,NFB,NEND,A2,ERR2,YOUT)
C     SUM RMS ERRORS FROM BOTH REGRESSIONS
      E(I)=ERR1+ERR2
```

```
      IF(NFB.GE.NMAX)GO TO 15
      GO TO 10
15    ER=E(1)
C     FIND MINIMUM ERROR
      DO 20 J=2,I
      IF(E(J).GT.ER)GO TO 20
      ER=E(J)
      IMIN=J
20    CONTINUE
C     RECALCULFORE SLOPES FOR MINIMUM ERROR
      NFB=NMIN+IMIN
      CALL LINREG(X,Y,1,NFB,A1,B1,ERR1,YOUT)
      CALL CLR(X,Y,NFB,NEND,A2,ERR2,YOUT)
      FB=NFB*TLF
      ER=ERR1+ERR2
      RETURN
      END
C
C
C
      SUBROUTINE ONESLP(X,S,A1,B1,ER,CLIF,CUTOF)
C
C     SINGLE SLOPE REGRESSION
C
C         X -- ARRAY OF HARMONIC FREQUENCIES
C         S -- ARRAY OF SPECTRAL COMPONENTS
C        A1 -- SLOPE (DB/DEC)
C        B1 -- POWER LEVEL INTERCEPT (DB)
C        ER -- TOTAL RMS ERROR
C      CLIF -- NOISE CUTOFF FREQUENCY (HZ)
C     CUTOF -- NOISE CUTOFF LEVEL (DB)
C
      DIMENSION X(1),S(1),YOUT(1024)
      DATA NMFM1/1023/
      TLF=10./2048.
C     CALCULATE SLOPE
      CALL LINREG(X,S,1,1023,A1,B1,ER,YOUT)
C     FIND NOISE CUTOFF FREQUENCY
      DO 10 I=1,NMFM1
10    IF(YOUT(I).LT.CUTOF)GO TO 20
      CLIF=5.
      GO TO 30
20    CLIF=I*TLF
C     RECALCULATE SLOPE USING SPECTRAL COMPONENTS
C     BELOW NOISE CUTOFF FREQUENCY
30    CALL LINREG(X,S,1,I,A1,B1,ER,YOUT)
      RETURN
      END
C
C
C
      SUBROUTINE LINREG(X,Y,NLO,NHI,SLOPE,YINT,ER,YOUT)
C
C     LINEAR REGRESSION
C
```

```
C          X -- ABSCISSA ARRAY
C          Y -- ORDINATE ARRAY
C        NLO -- STARTING INDEX OF REGRESSION
C        NHI -- ENDING INDEX OF REGRESSION
C      SLOPE -- SLOPE OF Y VERSUS X
C       YINT -- Y INTERCEPT
C         ER -- RMS ERROR
C       YOUT -- ARRAY OF SLOPE AND Y INTERCEPT LINE
C               (YOUT=SLOPE*X+YINT)
C
      DIMENSION X(1),Y(1),YOUT(1024)
      DATA X0/-2./
      XSUM=0.
      YSUM=0.
      XYSUM=0.
      X2SUM=0.
C     CALCULATE SLOPE AND Y INTERCEPT
      DO 1 I=NLO,NHI
      XSUM=XSUM+X(I)-X0
      YSUM=YSUM+Y(I)
      XYSUM=XYSUM+(X(I)-X0)*Y(I)
    1 X2SUM=X2SUM+(X(I)-X0)**2
      EX=XSUM/(NHI-NLO+1)
      EY=YSUM/(NHI-NLO+1)
      EXY=XYSUM/(NHI-NLO+1)
      EX2=X2SUM/(NHI-NLO+1)
      SLOPE=(EXY-EX*EY)/(EX2-EX*EX)
      YINT=EY-SLOPE*EX
C     CALCULATE RMS ERROR
      ERRSUM=0.
      DO 2 I=NLO,NHI
      YOUT(I)=SLOPE*(X(I)-X0)+YINT
    2 ERRSUM=ERRSUM+((YOUT(I)-Y(I))**2)
      ER=ERRSUM/(NHI-NLO+1)
      ER=SQRT(ER)
      RETURN
      END
C
C
C
      SUBROUTINE CLR(X,Y,NLO,NHI,SLOPE,ER,YOUT)
C
C     CONSTRAINED LINEAR REGRESSION
C
C          X -- ABSCISSA ARRAY
C          Y -- ORDINATE ARRAY
C        NLO -- STARTING INDEX
C        NHI -- ENDING INDEX
C      SLOPE -- SLOPE OF Y VERSUS X
C         ER -- RMS ERROR
C       YOUT -- ARRAY OF SLOPE LINE
C
      DIMENSION X(1),Y(1),YOUT(1024)
      COMMON/SET1/NFREQ,NRATE,TLF
      X0=NLO*TLF
```

```
      X0=ALOG10(X0)
      Y0=YOUT(NLO)
      XSUM=0.
      X2SUM=0.
      XYSUM=0.
C     CALCULATE SLOPE
      DO 10 I=NLO,NHI
      XSUM=XSUM+X(I)-X0
      X2SUM=X2SUM+(X(I)-X0)**2
10    XYSUM=XYSUM+(X(I)-X0)*Y(I)
      EX=XSUM/(NHI-NLO+1)
      EX2=X2SUM/(NHI-NLO+1)
      EXY=XYSUM/(NHI-NLO+1)
      SLOPE=(EXY-EX*Y0)/EX2
C     CALCULATE RMS ERROR
      ERRSUM=0.
      DO 20 I=NLO,NHI
      YOUT(I)=SLOPE*(X(I)-X0)+Y0
20    ERRSUM=ERRSUM+(YOUT(I)-Y(I))**2
      ER=ERRSUM/(NHI-NLO+1)
      ER=SQRT(ER)
      RETURN
      END
C
C
```

APPENDIX B

REFRACTIVITY OF AIR IN THE PRESENCE OF WATER VAPOR AND OXYGEN

Refractivity, N, can be expressed in general as

$$N = N_o + \sum_i S_i F_i' + N_w' + j\left(\sum_i S_i F_i'' + N_w''\right) \text{ ppm} \qquad (25)$$

where summations are over all spectral lines and

N_o = frequency-independent refractivity (ppm)
S^o = line strength (KHz)
F = line shape factor (GHz^{-1})
N_w = non-resonant refractivity due to water vapor (ppm).

The frequency-independent refractivity is given by[19]

$$N_o = 77.67 \frac{P}{T} + 71.7 \frac{P_w}{T} + 3.744 \times 10^5 \frac{P_w}{T^2} \text{ (ppm)} \qquad (26)$$

where P = dry air pressure (mbars)
P_w = water vapor pressure (mbars)
T^w = temperature (^oK)

Water Vapor. The resonance lines for water vapor are described by

$$F_1' = \frac{f}{f_1}\left[\frac{f_1 - f}{(f_1-f)^2+\gamma_1^2} - \frac{f_1 + f}{(f_1+f)^2+\gamma_1^2}\right] (GHz^{-1}) \qquad (27)$$

$$F_1'' = \frac{f}{f_1}\left[\frac{\gamma_1}{(f_1-f)^2+\gamma_1^2} + \frac{\gamma_1}{(f_1+f)^2+\gamma_1^2}\right] (GHz^{-1}) \qquad (28)$$

The only water vapor line relevant to this study is characterized by

$$S_1 = 4.465 \times 10^7 \, P_w T^{-3.5} \, e^{-643/T} \quad (kHz)$$

$$\gamma_1 = 0.0861 \, (P + 4.8 \, P_w) T^{-0.6} \quad (GHz)$$

$$f_1 = 22.235 \text{ (GHz)}$$

The nonresonant contributions to refractivity are

$$N'_w = 2432\ P_w\ f^{0.1} T^{-1.2} \qquad \text{(ppm)} \qquad (29)$$

$$N''_w = 1.1\ P\ P_w f^{1.3} T^{-3.5} \qquad \text{(ppm)} \qquad (30)$$

Oxygen. Since there are numerous oxygen lines it is convenient to describe these lines by a single line characterized by[20]

$$F'_2 = \frac{f_2 - f}{\gamma_2^2} \frac{\left(\frac{P}{1013.25}\right)\left(\frac{300}{T}\right)^2}{\left[1 + \left(\frac{f_2 - f}{\gamma_2}\right)^2\right]} \qquad (31)$$

$$F''_2 = \frac{1}{\gamma_2} \frac{\left(\frac{P}{1013.25}\right)\left(\frac{300}{T}\right)^2}{\left[1 + \left(\frac{f_2 - f}{\gamma_2}\right)^2\right]} \qquad (32)$$

along with the parameters

$S_2 = 5.22$ kHz

$\gamma_2 = 3.92$ GHz

$f_2 = 60.0$ GHz

Derivatives of the Refractivity

To compute the lower break frequency of the spectrum of amplitude fluctuations it is desirable to obtain an expression for the derivatives of the real and imaginary parts of the refractivity with respect to temperature.

a) The real part of the refractivity is found from Equation (25) as

$$\mathrm{Re}(N) = N_o + \sum_{i=1}^{2} S_i F'_i + N'_w \qquad (33)$$

Each of the terms in the above equation is temperature dependent. The derivative of Re(N) with respect to temperature is found as

$$\frac{\partial \, Re(N)}{\partial T} = \frac{\partial N_o}{\partial T} + F_1' \frac{\partial S_1}{\partial T} + S_1 \frac{\partial F_1'}{\partial T} + S_2 \frac{\partial F_2'}{\partial T} + \frac{\partial N_w'}{\partial T} \quad (ppm/k) \tag{34}$$

where

$$\frac{\partial N_o}{\partial T} = -77.67 \frac{P}{T^2} - 71.7 \frac{P_w}{T^2} - 7.488 \times 10^5 \frac{P_w}{T^3} \quad (ppm/k)$$

$$\frac{\partial S_1}{\partial T} = -1.563 \times 10^8 \, P_w T^{-4.5} \, e^{-643/T} + 2.871 \times 10^{10} \, P_w T^{-5.5} e^{-643/T} \quad (GHz/k)$$

$$\frac{\partial F_1'}{\partial T} = 2\gamma_1 \left(\frac{f}{f_1}\right) \frac{\partial \gamma_1}{\partial T} \left\{ \frac{f_1+f}{[(f_1+f)^2+\gamma_1^2]^2} - \frac{f_1-f}{[(f_1-f)^2+\gamma_1^2]^2} \right\} (GHz^{-1}\text{-}k^{-1})$$

$$\frac{\partial \gamma_1}{\partial T} = -0.05166 \, (P+4.8 \, P_w) T^{-1.6}$$

$$\frac{\partial F_2'}{\partial T} = -1.8 \times 10^5 \left(\frac{f_2-f}{\gamma_2^2}\right) \frac{\left(\frac{P}{1013.25}\right)}{\left[1 + \left(\frac{f_2-f}{\gamma_2}\right)^2\right]} \frac{1}{T^3} \quad (GHz^{-1}\text{-}k^{-1})$$

$$\frac{\partial N_w'}{\partial T} = -2918 \, P_w f^{0.1} \, T^{-2.2} \quad (ppm/k)$$

b) The imaginary part of the refractivity is found from Equation (25) as

$$Im(N) = \sum_{i=1}^{2} S_i F_i'' + N_w'' \quad (ppm) \tag{35}$$

The derivative of Im(N) with respect to temperature is found as

$$\frac{\partial \mathrm{Im}(N)}{\partial T} = F_1'' \frac{\partial S_1}{\partial T} + S_1 \frac{\partial F_1''}{\partial T} + S_2 \frac{\partial F_2''}{\partial T} + \frac{\partial N_w''}{\partial T} \quad \text{(ppm/k)} \qquad (36)$$

where

$$\frac{\partial F_1''}{\partial T} = \frac{\partial \gamma_1}{\partial T}\left\{\frac{F_1''}{\gamma_1} - 2\left(\frac{f}{f_1}\right)\left[\frac{\gamma_1^2}{[(f_1-f)^2+\gamma_1^2]^2} + \frac{\gamma_1^2}{[(f_1+f)^2+\gamma_1^2]^2}\right]\right\}$$

$$(\mathrm{GHz}^{-1}\text{-}\mathrm{k}^{-1})$$

$$\frac{\partial F_2''}{\partial T} = \frac{-1.8\times10^{5}}{\gamma_2} \frac{\left(\frac{P}{1013.25}\right)}{\left[1+\left(\frac{f_2-f}{\gamma_2}\right)^2\right]} \frac{1}{T^3} \quad (\mathrm{GHz}^{-1}\text{-}\mathrm{k}^{-1})$$

$$\frac{\partial N_w''}{\partial T} = -3.85\ PP_w\ f^{1.3}\ T^{-4.5} \quad \text{(ppm/k)}$$

APPENDIX C

SPECTRAL SLOPE OF A RANDOM TELEGRAPH SIGNAL

It is desirable to find the slope of the power density spectrum of a random telegraph signal (which is similar to random toggling of the least significant bit of an A/D converter).

From Papoulis[15], the autocorrelation function, R, of a random telegraph signal is exponentially damped as

$$R(\tau) = e^{-2\lambda|\tau|} \tag{37}$$

where τ is the lag time and λ is the occurrence rate. The power density spectrum, $S(\omega)$, is the Fourier Transform of $R(\tau)$,

$$S(\omega) = \frac{4\lambda}{4\lambda^2+\omega^2} \tag{38}$$

The spectral slope is

$$\frac{dS(\omega)}{d\omega} = \frac{-8\lambda\omega}{(4\lambda^2+\omega^2)^2} \tag{39}$$

An appropriate value of λ can be obtained from Figure 28 of Chapter IV. There are approximately 110 bit changes in the 204.8 second sample which gives a value of 110/204.8 = 0.54 for λ.

If the spectral slope is evaluated in the 0.25 Hz to 0.5 Hz region, $\lambda \approx \omega$ and the spectral shape is approximately

$$\frac{dS(\omega)}{d\omega} \approx \frac{-8}{25\omega^2} \tag{40}$$

Thus, the spectral slope of a waveform consisting of random bit toggling is -20 dB/decade, which is 6.7 dB/decade flatter than the spectral slope due to a Kolomogorov turbulence spectrum.

APPENDIX D

SPECTRAL SLOPE OF STRONG FLUCTUATIONS

Ishimaru[11] has considered the effect of strong fluctuations on the mutual coherence function, Γ. The mutual coherence function is similar to the covariance function defined in Equation (5) except that Γ is defined in terms of the specific intensity, I, instead of the log amplitude fluctuations, i.e.,

$$\Gamma(x) = \int_L I(x,\bar{s}) e^{-j\bar{k}\cdot\bar{s}} \, d\bar{s} \tag{41}$$

where x is the spatial lag distance, $\bar{s}$ is the path vector, and the integration is along the path, L.

If the turbulence is strong, x is large, and Taylor's hypothesis is valid then for a spherical wave

$$\Gamma(x) \sim \frac{F(x)}{x^2} \tag{42}$$

where

$$F(x) = \exp\{-1.46k^2(v\tau)^{5/3} \int_0^x C_n^2(x')dx'\} ,$$

and v is the perpendicular wind speed, τ is the lag time and C_n^2 is the refractive index structure constant.

Because Taylor's hypothesis is assumed, the product $v\tau$ is slowly varying; furthermore, changes in $v\tau$ do not have a significant effect on F(x). If it is assumed that $v\tau \leq 10$ then $F(x) \sim 1$, and the Fourier transform of $\Gamma(x)$ is simply

$$S(\omega) = -\pi\omega, \ \omega > 0 \tag{43}$$

which is the power density spectrum of the strong fluctuations. Thus, the slope of the strong fluctuations' spectrum is 0 dB/decade.

REFERENCES

1. D. M. J. Davasirvatham and D. B. Hodge, "Amplitude Scintillations on Earth-space Propagation Paths at 2 and 30 GHz," Report 4299-4, March 1977, The Ohio State University Electro-Science Laboratory, Department of Electrical Engineering; prepared under Contract NAS5-22575 for NASA-Goddard Space Flight Center.

2. H. G. Booker and W. E. Gordon, "A Theory of Radio Scattering in the Troposphere," Proc. I.R.E., vol. 36, April, 1950, pp. 401-412.

3. F. Villars and V. F. Weisskopf, "On the Scattering of Radiowaves by Turbulent Fluctuations of the Atmopshere," Proc. I.R.E., vol. 43, October, 1955, pp. 123-1239.

4. R. A. Silverman, "Fading of Radio Waves Scattered by Dielectric Turbulence," J. of Appl. Phys., vol. 28, April, 1957, pp. 506-511.

5. A. D. Wheelon, "Relation of Radio Measurements to the Spectrum of Tropospheric Dielectric Fluctuation," J. of Appl. Phys., vol. 28, June, 1957, pp. 684-693.

6. Armel Picquenard, Radio Wave Propagation, John Wiley and Sons: New York and Toronto, 1974, Ch. 2.

7. V. I. Tatarskii, Wave Propagation in a Turbulent Medium, R. A. Silverman, Transl., McGraw-Hill: New York, 1961.

8. Akira Ishimaru, "Temporal Frequency Spectra of Multi-frequency Waves in Turbulent Atmosphere," I.E.E.E. AP-20, No. 1, January, 1972, pp. 10-19.

9. V. I. Tatarski, "The Effects of the Turbulent Atmosphere on Wave Propagation," transl. from Russian. Israel Program for Scientific Translations: Jerusalem, 1971.

10. W. Lee Robert and Jeffrey C. Harp, "Weak Scattering in Random Media, with Applications to Remote Probing," Proc. I.E.E.E., vol. 57, No. 4, April, 1969, pp. 375-406.

11. Akira Ishimaru, "Theory and Application of Wave Propagation and Scattering in Random Media," Proc. I.E.E.E., vol. 65, No. 7, July, 1977, pp. 1030-1061.

12. P. A. Mandics, R. W. Lee, and A. T. Waterman, Jr., "Spectra of Short-term Fluctuations of Line-of-Sight Signals: Electromagnetic and Acoustic," Radio Science, vol. 8, No. 3, March, 1973, pp. 185-201.

13. Akira Ishimaru, "Fluctuations of a Beam Wave Propagating through a Locally Homogeneous Medium," Radio Science, vol. 4, April, 1969, pp. 255-305.

14. R. H. Ott and M. C. Thompson, Jr., "Atmospheric Amplitude Spectra in an Absorption Region," I.E.E.E. Trans. Antennas Propagat., vol. AP-26, No. 2, March, 1978, pp. 329-332.

15. A. Papoulis, Probability, Random Variables, and Stochastic Processes, McGraw-Hill, New York, 1965, Ch. 9.

16. R. B. Blackman and J. W. Tukey, The Measurement of Power Spectra, Dover Publications, Inc., New York, 1958.

17. Warren D. Brown, "A Model for the Refractive Index Structure Constant at Microwave Frequencies," Sandia Laboratories, New Mexico, February, 1977.

18. W. I. Vogel, A. W. Straiton, and B. M. Fannin, "ATS-6 Ascending: Near Horizon Measurements over Water at 30 GHz," Radio Science, vol. 12, No. 5, September-October, 1977, pp. 757-765.

19. H. J. Liebe and G. G. Gimmestad, "Calculation of Clear Air EHF Refractivity," Radio Science, vol. 13, No. 2, March-April, 1978, pp. 245-251.

20. R. H. Ott and M. C. Thompson, Jr., "Characteristics of a Radio Link in the 55 to 65 GHz Range," I.E.E.E. Transactions on Ant. and Prop., AP-24, November, 1976, pp. 873-889.

21. A. Papoulis, The Fourier Integral and its Applications, McGraw-Hill: New York, 1962, Ch. 12.

ACKNOWLEDGMENTS

The authors wish to express special thanks to Dr. David M. Theobold for his numerous and fruitful ideas, especially those developed in Appendices C and D, given to them throughout the course of this work.

Thanks also go to Robert C. Taylor for his expert assistance during and after the experiment, to D. M. J. Devasirvatham for the preliminary data analysis which inspired this work, and to Dorothy M. McGinty for typing the manuscript.